Localized surface plasmon resonance based nanocube-nanosphere dimer biosensor

Thesis submitted in partial fulfilment of the requirements for the degree of Bachelor of Science in Applied Physics and Electronics

by
Arik Rafiquddin Ahmed

Department of Mathematics and Natural Sciences
BRAC University

Declaration

I, hereby, declare that the thesis "Localized surface plasmon resonance based nanocube-nanosphere dimer" is based on self-derived results. Materials that support my work by other researchers are mentioned in the reference section. This thesis, neither in whole nor in part, has been previously submitted for any degree.

_____

Candidate

Arik Rafiquddin Ahmed

ID: 13115002

_____

Certified by

Avijit Das

Supervisor

Lecturer

Department of EEE

BRAC University, Dhaka

Acknowledgement

Many thanks are in order for the successful completion of this paper, there was a lot that lead up to this moment.

First of all to my supervisor Avijit Das Sir who would provide thorough guidance and was always there for any queries I had, often during the most inconvenient of times. I consider myself lucky that he agreed to be the supervisor of my thesis even though he is from a different department.

Then there is the chairperson of the MNS department Dr. A.A. Ziauddin Ahmad Sir who has provided a great learning environment for me and many others and has been endlessly patient and considerate during this whole process.

A special mention must go to certain faculty members such as Md. Lutfor Rahman Sir and Dr. Tafazzal Hussain Sir whose classes I have always enjoyed who have always managed to pique my curiosity.

Also I must acknowledge many of my teachers from my younger days such as Fahim Sir, Riad Sir, etc. who helped lay my educational foundations.

And last but not least I am eternally grateful to my parents and other immediate family members for always being there for me and encouraging me to pursue my goals.

Abstract

For this paper, the Localized Surface Plasmon Resonance (LSPR) properties of bimetallic nanoparticles in the shape of a nanocube-nanosphere and consisting of Drude metals was analysed. The refractive index based plasmonic bio-sensing with nanocube-nanosphere dimers was studied through the illumination of a broadband beam at normal. The power absorption curves and electric field graphs for different material combinations between the nanocube and nanosphere were analysed to select the best material combination, which was found as silver nanocube-silver nanosphere. Using that combination, the gap between the nanocube and nanosphere was varied to find out the optimal gap, which was found as 1 nm. Taking that gap and material combination, the physical dimensions of the nanocube and nanosphere were varied and the best nanocube-nanosphere size was selected which was a nanocube of side length 20 nm and a nanosphere of radius 12.5 nm. The refractive index sensitivity was analysed in terms of different dielectric media. The sensitivity of the nanocube-nanosphere was also calculated in the presence of Lysozyme (Lys), Human Serum Albumin (HSA), Human gamma-immunoglobulin (IgG) and Human Fibrinogen (Fb) protein samples. Therefore, a comparative analysis was done to highlight how well the dimer performed as a biosensor in certain conditions. All of these processes were simulated using the software FDTD solutions by Lumerical.

Table of Contents

List of Figures

List of Tables

1. Introduction

Nanoparticles are defined as objects where at least one dimension has a magnitude below 100 nm. As particles approach the nanoscale, their properties start to differ from that of bulk materials and become more size-dependent. These unique properties are the reason why nanoparticles have applications in many different fields. In this paper, the main focus will be on localised surface plasmon resonance (LSPR) in nanocube-nanosphere dimers.

1.1 A short introduction to nano-plasmonics

Plasmonics is the transfer of information in nanoscale structures by means of plasmons.
The first person to predict the existance of surface plasmons was Rufus Richie in the year 1957. The research on this topic was later continued by T. Turbadar in the 1950s and 1960s, and Heinz Raether, E. Kretschmann, and A. Otto in the 1960s and 1970s.

Light scattering of minute nanoparticles is a fascinating research interest for a range of applications. It starts from the energy sector, where it is used for increasing the efficiency of solar cells, and goes all the way to the medical sector, where it plays a role in the imagery and drug delivery systems. The mode by which these nanoparticles scatter light is extremely crucial to the research. Light scattering is the reduction or weakening of a beam of light by particles, either by absorption or by scattering. The summation of these two parts is known as the **extinction** [1].

Nanoplasmonics is the study of optical phenomena in the nanoscale vicinity of metal surfaces [2]. Due to the excitation of localized surface plasmons, noble-metal nanoparticles that are of size smaller than the wavelength of light in the visible region, show strong resonances for light scattering and absorption. When the frequency of the light matches that of the vibrating surface electrons, the light resonantly energizes and causes combined oscillation of the conduction electrons of the metal nanoparticle, which in turn acts as a regular dipole. Its resonance frequency is strongly dependent on the shape of the particle and the dielectric environment (which we will try to show in our thesis paper). This phenomenon enables us to tune the colour of the beam throughout the visible region and slightly into the near-infrared (IR) region of the electromagnetic spectrum, while keeping the size of the particle well below the 100 nm range [3].

Historically significant applications of this phenomenon include the formation of coloured glass with metal nanoparticle dopants. A dopant, otherwise known as a doping agent, is a trace impurity element that is inserted into a substance in very low concentrations to alter the electrical or optical properties of the substance. More modern applications that deal with a single nanoparticle involve the tagging of biomolecules, improvement of light emission from nanoscale photon sources, and biomolecular sensing. All of these properties exploit the fact that metal nanoparticles enable nano-concentration of light below the diffraction limit around

the particle surface at their dipolar resonant frequencies, and feature resonantly enhanced absorption and scattering cross-sections [3].

When carrying out practical experiments involving this phenomenon, we must consider processes such as Electron Beam Lithiography or Focused Ion Beam Milling to produce the metal nanoparticles. To ensure that the particles have accurate dimensions and shapes, Scanning Electron Microscope (SEM) imaging is necessary. Transmission Electron Microscopy (TEM) might be used to disentangle the properties of different plasmonic modes [3].

1.2 Applications in the medical sector of Surface Plasmon Resonance

The refractive index of the surrounding medium is one of the determinants for how a plasmonic interaction between metal nanoparticles takes place. Since the refractive index of a medium often corresponds to the presence of certain chemicals and/or substances, if we can deduce the refractive index of that medium by observing the surface plasmon resonance then we can go on to deduce the identity of the substances present in that medium. Hence surface plasmon resonance can be an effective tool for biological, chemical and medical sensing and recognition applications. To carry this out, metal nanoparticles can be made sensitive to unique sorts of biomolecules amid functionalization and certain substances will cause huge shifts in localised surface plasmon resonance [4].

Plasmonic interaction between metal nanoparticles is also affected by the separation between them. As a result, precise measurements of the plasmon resonance wavelength of metal particle assemblies functionalized with biomolecules can be used as a molecular-scale ruler that operates over a length of scale much larger than that in the fluorescence energy transfer metrology that is regularly used in biology. Practical usage of this concept is adopted in systems biology, for example, imaging of the motion of molecular motors or of structural changes in proteins and in DNA [4].

Another example for a promising application is the use of particles composed of a dielectric core and a metallic shell in cancer treatment. When these particles are injected into the human body, they are selectively bound to malicious (harmful or mutated) cells. This is when laser sterilization at a precisely engineered plasmon resonance wavelength is used to heat the particles and finally destroy the cells. [4]

2. Physics behind LSPR

2.1 Surface plasmon resonance and localized surface plasmon resonance

Surface plasmons (SP)

Surface plasmons are coherent delocalized electron oscillations that exist at the interface between any two materials where the real part of the dielectric constant changes sign across the interface (e.g. a metal-dielectric interface). There are evanescent waves on both sides of the interface.

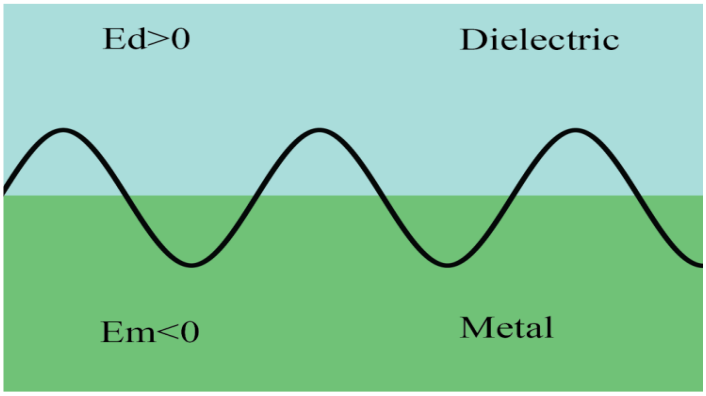

Figure 2.1 Surface plasmon

E_d = Permittivity of the dielectric
E_m = Permittivity of the metal

2.2 Evanescent waves

An evanescent wave is a near field wave with an intensity that exhibits exponential decay without absorption as a function of distance from the boundary at which the wave was formed. This means that the energy is confined in a small area in that wave.
There is decay on both sides of the interface and the wave only propagates in the longitudinal direction.

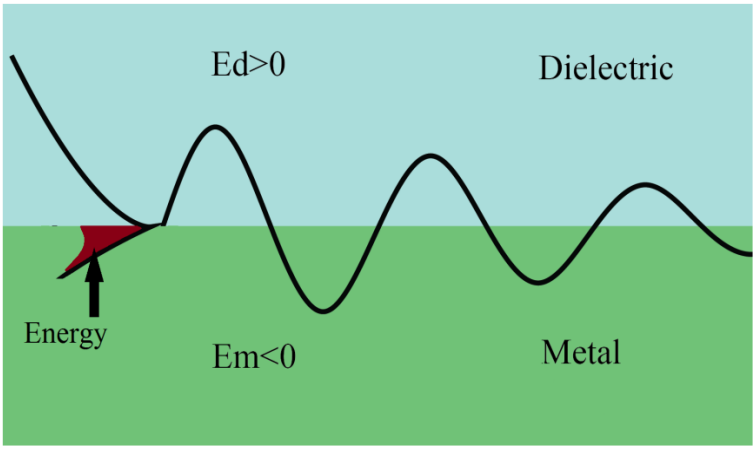

Figure 2.2 Evanescent wave

Surface plasmons have lower energy than bulk (or volume) plasmons which quantize the longitudinal electron oscillations about positive ion cores within the bulk of an electron cloud or plasma. The charge motion in an SP creates electromagnetic fields both inside and outside the metal. The total excitation, i.e. the charge motion and the associated electromagnetic field, is called a surface plasmon (or surface plasmon polariton, SPP) at a planar interface, or a localized surface plasmon for a small particle.

2.3 Surface plasmon resonance (SPR)

Surface plasmon resonance is the resonant oscillation of conduction electrons at the interface between negative (Em<0) and positive (Ed>0) permittivity material stimulated by incident light. When the frequency of the incident light is the same as the natural frequency of the surface electrons, the resonance condition is established, forcing the electrons to oscillate against the restoring force of the positive nuclei. Surface plasmon resonance in subwavelength scale nanostructures can be polaritonic or plamonic in nature [3].

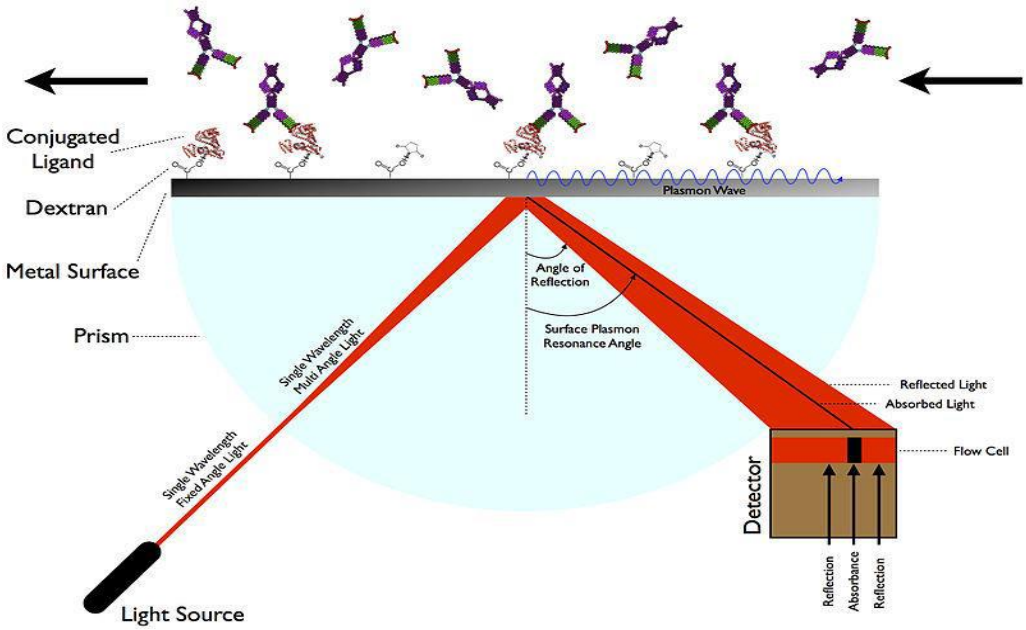

Figure 2.3 Surface Plasmon Resonance

SPR is the excitation of a coupled state between photons and plasma oscillations at the interface between a metal and a dielectric [5].

- Radiative surface plasmons are coupled with propagating electromagnetic waves
- Non-radiative surface plasmons do not couple with propagating electromagnetic waves
- Surface plasmon polarizations (SPPs) are always non-radiative for perfectly flat surfaces

In contrary to conventional wave guides, field on both sides are always evanescent.

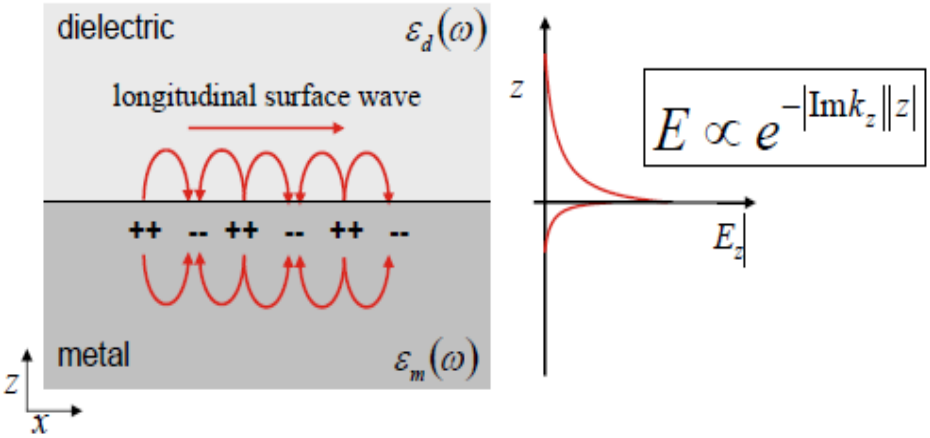

Figure 2.4 Schematic of Surface Plasmon Resonance [5]

2.4 Localized surface plasmon resonance (LSPR)

This paper is mainly concerned with localized surface plasmon resonance (LSPR).
A localized surface plasmon (LSP) is the result of the confinement of a surface plasmon in a nanoparticle of size comparable or smaller than the wavelength of the light in the visible range or the light used to excite the plasmon. LSP has two important effects:

- Electric fields near the particle's surface are greatly enhanced. This enhancement falls off quickly if the distance from the surface is increased.
- The particle's optical absorption has a maximum at the plasmon resonant frequency. For noble metal nanoparticles, this occurs at visible wavelengths. For semiconductor nanoparticles, the maximum optical absorption occurs in the near-infrared or mid-infrared region.

Localized surface plasmons are **non-propagating** excitations of the conduction electrons of metallic nanostructures coupled to the electromagnetic field. These modes generate naturally from the scattering problem of a small, sub-wavelength conductive nanoparticle in an oscillating electromagnetic field. An operative restoring force is exerted on the driven electrons by the curved surface of the nanoparticle. As a result, a resonance arises, leading to field amplification on both inside and in the near-field zone outside the particle. This resonance is called **localized surface plasmon resonance**. Another significance of the curved surface is that the plasmon resonances can be generated by direct light illumination [3].

For gold and silver nanoparticles, the resonance falls into the visible range of the electromagnetic spectrum. It is solely because of this that the bright colors are displayed by particles both in transmitted and reflected light, due to resonantly improved absorption and

scattering. This application has made itself very useful for many centuries, for example, in the staining of glass in windows or ornamental cups [3].

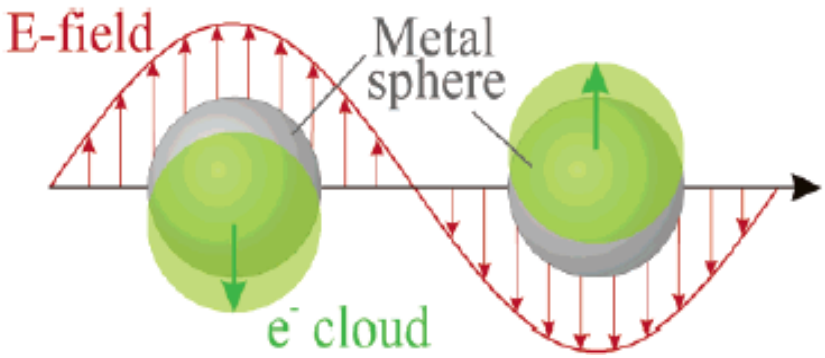

Figure 2.5 Schematic of Localized Surface Plasmon oscillation of a sphere, showing the displacement of the conduction electron charge cloud relative to the nuclei. [1]

2.5 LSPR in a metal sphere

The interaction of a particle of size *d* with the electromagnetic field can be analyzed by using the **Quasi-Static** approximation, given that $d<<\lambda$, that is, the particle is far smaller than the wavelength of the incident light surrounding the medium. In a case like this, the phase of the harmonically oscillating electromagnetic field is virtually constant over the particle volume. Hence, it is possible to calculate the spatial field distribution by assuming the simplified problem of a particle in an electrostatic field. Once the field distributions are acknowledged, the harmonic time dependence can then be added to the solution. This lowest-order estimation of the full scattering problem describes the optical properties of nanoparticles of proportions below 100 nm, effectively for many purposes [3].

We start with the simplest geometry for an analytical treatment: a homogeneous, isotropic sphere of radius *a*, positioned at the origin in a uniform, static electric field, $\mathbf{E} = E_0\,\hat{}\mathbf{z}$, the surrounding medium is isotropic and non-absorbing with dielectric constant εm, and the field lines are parallel to the z-direction at an adequate amount of distance from the sphere. The dielectric response of the sphere is further described by the dielectric function $\varepsilon\ (\omega)$, which we consider as a simple complex number ε for the time being [3].

Approaching from an electrostatic point of view, we are concerned in a solution of the **Laplace equation** for the potential, $\nabla 2\Phi = 0$, from which we will be able to calculate the electric field, $\mathbf{E} = -\nabla\Phi$. Due to the azimuthal symmetry of the problem, the general solution is of the form:

$$\Phi\,(r,\theta) = \sum_{l=0}^{\infty}\left[A_l r^l + B_l r^{-(l+1)}\right] P_l\,(\cos\theta),$$

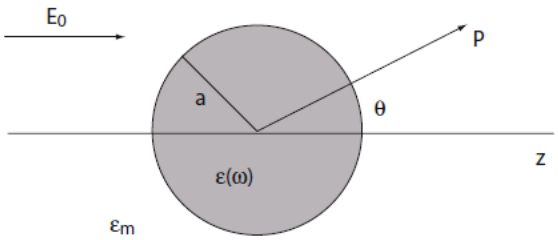

Figure 2.6 Sketch of a homogeneous sphere in an electrostatic field [2]

where $P_l(\cos\theta)$ are the Legendre Polynomials of order l, and θ the angle between the position vector **r,** at point P and the z-axis. Due to the requirement that the potentials remain finite at the origin, the solution for the potentials Φ_{in} inside and Φ_{out} outside the sphere can be written as:

$$\Phi_{\text{in}}(r,\theta) = \sum_{l=0}^{\infty} A_l r^l P_l(\cos\theta)$$

$$\Phi_{\text{out}}(r,\theta) = \sum_{l=0}^{\infty} \left[B_l r^l + C_l r^{-(l+1)}\right] P_l(\cos\theta).$$

The coefficients A_l, B_l and C_l can now be determined form the boundary conditions at $r \to \infty$ and at the sphere surface $r = a$. The requirement that $\Phi_{in} \to -E_0 z = -E_0 r \cos\theta$ as $r \to \infty$ demands that $B_l = -E_0$ and $B_l = 0$ for $l \neq 1$. The remaining coefficients A_l and C_l are defined by the boundary conditions at $r = a$. Equality of the tangential components of the electric field demands that

$$-\frac{1}{a}\frac{\partial \Phi_{\text{in}}}{\partial \theta}\bigg|_{r=a} = -\frac{1}{a}\frac{\partial \Phi_{\text{out}}}{\partial \theta}\bigg|_{r=a},$$

And the equality of the normal components of the displacement field

$$-\varepsilon_0 \varepsilon \frac{\partial \Phi_{\text{in}}}{\partial r}\bigg|_{r=a} = -\varepsilon_0 \varepsilon_{\text{m}} \frac{\partial \Phi_{\text{out}}}{\partial r}\bigg|_{r=a}.$$

Application of these boundary conditions leads to $A_l = C_l = 0$ for $l \neq 1$, and via the calculation of the remaining coefficients A_l and C_l, the potentials evaluate to:

$$\Phi_{\text{in}} = -\frac{3\varepsilon_m}{\varepsilon + 2\varepsilon_m} E_0 r \cos\theta$$

$$\Phi_{\text{out}} = -E_0 r \cos\theta + \frac{\varepsilon - \varepsilon_m}{\varepsilon + 2\varepsilon_m} E_0 a^3 \frac{\cos\theta}{r^2}.$$

It is interesting to interpret the w=equation physically: Φ_{out} describes the superposition for the applied field and that of a dipole located at the particle center. We can rewrite Φ_{out} by introducing the dipole moment **p** as:

$$\Phi_{\text{out}} = -E_0 r\cos\theta + \frac{\mathbf{p}\cdot\mathbf{r}}{4\pi\varepsilon_0\varepsilon_m r^3}$$

$$\mathbf{p} = 4\pi\varepsilon_0\varepsilon_m a^3 \frac{\varepsilon-\varepsilon_m}{\varepsilon+2\varepsilon_m}\mathbf{E}_0.$$

Therefore, we see that the applied field introduces a dipole moment inside the sphere of magnitude proportional to $|\mathbf{E}_0|$. If we introduce the polarisability *a*:

$$\alpha = 4\pi a^3 \frac{\varepsilon-\varepsilon_m}{\varepsilon+2\varepsilon_m}.$$

This equation is the central result of this section, the complex polarisability of a small sphere of sub-wavelength diameter in the electrostatic approximation. We note that it shows the same functional form as the Clausius-Mossotti relation.

The following figure (Fig. 2.7) shows the absolute value and phase of *a* with respect to frequency ω (in energy units) for a dielectric constant varying as $\varepsilon(\omega)$ of the Drude form, in this case fitted to the dielectric response of silver [Johnson and Christy, 1972]. It is obvious that the polarisability experiences a resonant improvement under the condition that $|\varepsilon + 2\varepsilon m|$ is a minimum, which for the case of small or slowly varying $I_m[\varepsilon]$ around the resonance simplifies to:

$$\text{Re}\,[\varepsilon\,(\omega)] = -2\varepsilon_m.$$

This relationship is called the Fröhlich condition and the associated mode (in an oscillating field) the *dipole surface plasmon* of the metal nanoparticle. For a sphere consisting of a Drude metal with a dielectric function located in air, the Fröhlich criterion is met at the frequency $\omega_0=\omega_p/\sqrt{3}$, which further expresses the strong dependence of the resonance frequency on the dielectric environment: The resonance red shifts as ε_m is increased. Metal nanoparticles are thus the ideal platforms for optical sensing of change in refractive index.

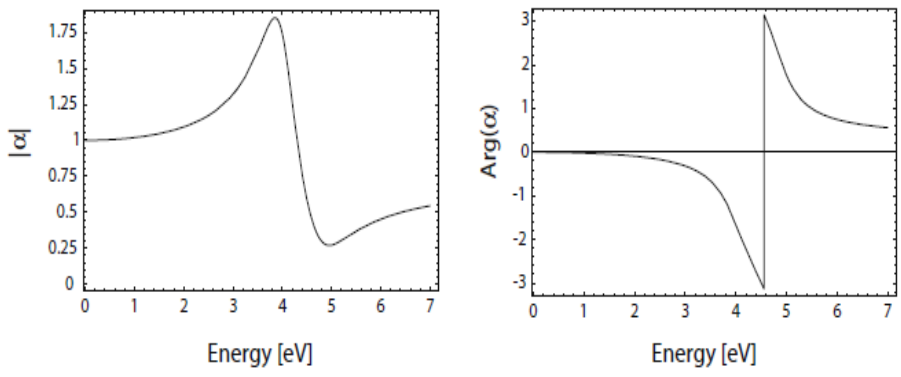

Figure 2.7 Absolute value and field polarizability α of a sub-wavelength metal nanoparticle with respect to frequency of the driving field (expressed as eV units). Here, ε(ω) is taken as a Drude fit to the dielectric function of silver [Johnson and Christy. 1972].[2]

We note that the magnitude of α at resonance is limited by the incomplete vanishing of its denominator, due to $I_m[\varepsilon(\omega)] \neq 0$.

The distributions of the electric field $\mathbf{E} = -\nabla\Phi$ can be evaluated from the potentials to:

$$\mathbf{E}_{\mathbf{in}} = \frac{3\varepsilon_m}{\varepsilon + 2\varepsilon_m}\mathbf{E}_0$$
$$\mathbf{E}_{\mathbf{out}} = \mathbf{E}_0 + \frac{3\mathbf{n}\,(\mathbf{n}\cdot\mathbf{p}) - \mathbf{p}}{4\pi\,\varepsilon_0\varepsilon_m}\frac{1}{r^3}.$$

The resonance in α also implies a resonant enhancement of both the internal and dipolar fields. It is this field enhancement at the plasmon resonance on which many of the prominent applications of metal nanoparticles in optical devices and sensors rely.

We have been on the firm ground of electrostatics, which we will now leave and turn our attention to the electromagnetic fields radiated by a small particle excited at its plasmon resonance. For a small sphere $a << \lambda$, its representation as an ideal dipole is valid in the Quasi-Static regime, i.e. it allows for time-varying fields but neglects spatial retardation effects over the particle volume. Under plane-wave illumination with $\mathbf{E}(\mathbf{r}, t) = \mathbf{E}_0 e^{-i\omega t}$, the fields introduce an oscillating dipole moment $\mathbf{p}(t) = \varepsilon_0\varepsilon_m\alpha\mathbf{E}_0 e^{-i\omega t}$, with α given by the electrostatic result. The radiation of this dipole leads to *scattering* of the plane wave by the sphere, which can be represented as radiation by a point dipole.

It is useful to briefly review the basics of the electromagnetic fields associated with an oscillating electric dipole. The total fields $\mathbf{H}(t) = \mathbf{H}e^{-i\omega t}$ and $\mathbf{E}(t) = \mathbf{E}e^{-i\omega t}$ in the near immediate zones of a dipole can be written as:

$$\mathbf{H} = \frac{ck^2}{4\pi}(\mathbf{n}\times\mathbf{p})\frac{e^{ikr}}{r}\left(1 - \frac{1}{ikr}\right)$$

$$\mathbf{E} = \frac{1}{4\pi\,\varepsilon_0\varepsilon_m}\left\{k^2(\mathbf{n}\times\mathbf{p})\times\mathbf{n}\frac{e^{ikr}}{r} + [3\mathbf{n}\,(\mathbf{n}\cdot\mathbf{p}) - \mathbf{p}]\left(\frac{1}{r^3} - \frac{ik}{r^2}\right)e^{ikr}\right\},$$

With $k = 2\pi/\lambda$ and $\mathbf{n}$ the unit vector in the direction of the point P of interest. In the near zone $(kr << 1)$, the electrostatic result for the electric field is recovered,

$$\mathbf{E} = \frac{3\mathbf{n}\,(\mathbf{n}\cdot\mathbf{p}) - \mathbf{p}}{4\pi\,\varepsilon_0\varepsilon_m}\frac{1}{r^3}$$

And the accompanying magnetic field present for oscillating fields amounts to:

$$\mathbf{H} = \frac{i\omega}{4\pi}(\mathbf{n}\times\mathbf{p})\frac{1}{r^2}.$$

We can see that within the near field, the fields are predominantly electric in nature, since the magnitude of the magnetic field is about a factor $\sqrt{(\varepsilon_0/\mu_0)}\,(kr)$ smaller than that of the electric field. For static fields $(kr \to 0)$, the magnetic field vanishes.
In the opposite limit of the radiation zone, defined by $kr >> 1$, the dipole fields are of the well-known spherical-wave form:

$$\mathbf{H} = \frac{ck^2}{4\pi}(\mathbf{n}\times\mathbf{p})\frac{e^{ikr}}{r}$$
$$\mathbf{E} = \sqrt{\frac{\mu_0}{\varepsilon_0\varepsilon_m}}\mathbf{H}\times\mathbf{n}.$$

We will now leave this short summary of the properties of dipolar radiation. It is much more interesting from the view point of optics to note that another consequence of the resonantly enhanced polarisation α is a concomitant enhancement in the efficiency with which a metal nanoparticle scatters and absorbs light. The corresponding cross sections for scattering and absorption C_{sca} and C_{abs} can be calculated via the Poynting-vector determined from above [Bohren and Huffman, 1983] to:

$$C_{\text{sca}} = \frac{k^4}{6\pi}|\alpha|^2 = \frac{8\pi}{3}k^4a^6\left|\frac{\varepsilon-\varepsilon_m}{\varepsilon+2\varepsilon_m}\right|^2$$
$$C_{\text{abs}} = k\,\text{Im}\,[\alpha] = 4\pi k a^3\,\text{Im}\left[\frac{\varepsilon-\varepsilon_m}{\varepsilon+2\varepsilon_m}\right].$$

For small particles with $a << \lambda$, the efficiency of absorption scaling with a^3, dominates over the scattering efficiency, which scales with a^6. We point out that no explicit assumptions were made in our derivations so far that the sphere is indeed metallic. The expressions for the cross sections are thus valid also for the dielectric scatterers, and demonstrate a very important problem for practical purposes. Due to rapid scaling of $C_{\text{sca}} \propto a^6$, it is very difficult to pick out small objects from a background of larger scatterers. Imaging of nanoparticles with dimensions below 40 nm, are immersed in an background of light scatterers can thus usually only be achieved using photo-thermal techniques relying on the slower scaling of the absorption cross section with size. Equations also show that indeed for metal nanoparticles, both absorption and scattering (and thus extinction) are resonantly enhanced at the dipole particle plasmon resonance, i.e. when Frölich condition is met. For a sphere of volume V and dielectric function $\varepsilon = \varepsilon_1 + i\varepsilon_2$ in the Quasi-Static limit, the explicit expression for the extinction cross section $C_{\text{ext}} = C_{\text{abs}} + C_{\text{sca}}$ is:

$$C_{\text{ext}} = 9\frac{\omega}{c}\varepsilon_m^{3/2}V\frac{\varepsilon_2}{[\varepsilon_1+2\varepsilon_m]^2+\varepsilon_2^2}.$$

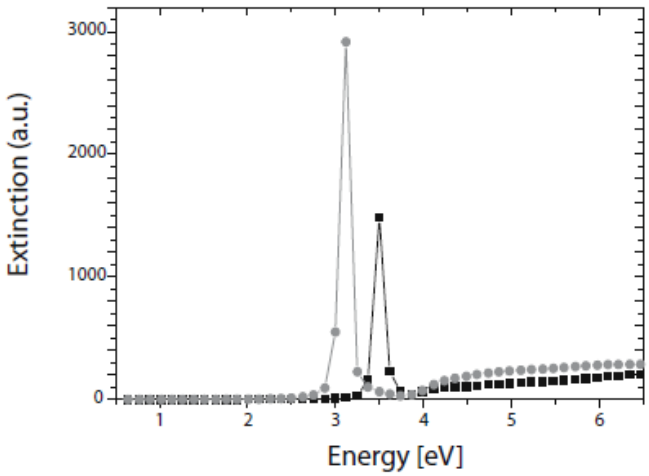

Figure 2.8 Extinction cross section for a sliver sphere in air (black curve) and in silica (grey curve), with the dielectric data taken from [Johnson and Christy, 1972] [3]

Figure 2.8 shows the extinction cross section of a sliver sphere in the Quasi-Static approximation calculated using this formula for immersion in two different media [3].

2.6 Difference between SPR and LSPR

Localized Surface Plasmon Resonance is produced by metal nanoparticles, especially silver and gold, whereas, Surface Plasmon Resonance is produced by a continuous film of gold.
LSPR produces a solid resonance absorbance peak in the visible range of light, with its position being exceptionally sensitive to the nearby refractive index encircling the molecule. In this manner, LSPR measures little changes in the wavelength of the absorbance position, as opposed to the angle as in conventional SPR [6].

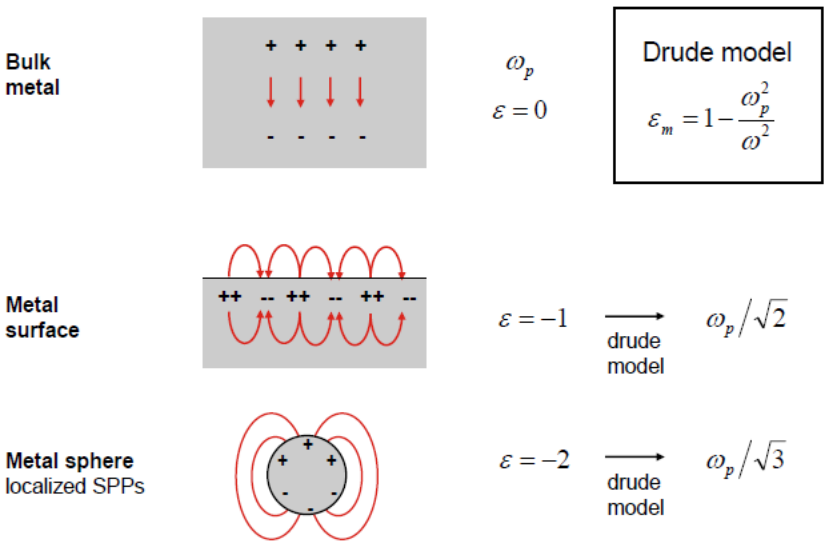

Figure 2.9 Plasmon resonance positions in vacuum [5]

Advantages of LSPR over SPR:

- The optical equipment required for LSPR is much less complicated since no prism is expected to couple the light, making the instrument smaller and more affordable
- Since the angle is not essential, the instrument is considerably more resistant to vibration and mechanical noise
- LSPR is not as sensitive to bulk refractive index changes, which causes mistakes in experimental information, since it has a much shorter electromagnetic field decay length
- No strict temperature control is required, making the instrument simpler to use
- The sensor chips can be made at a more reasonable cost
- Easier to use and sustain

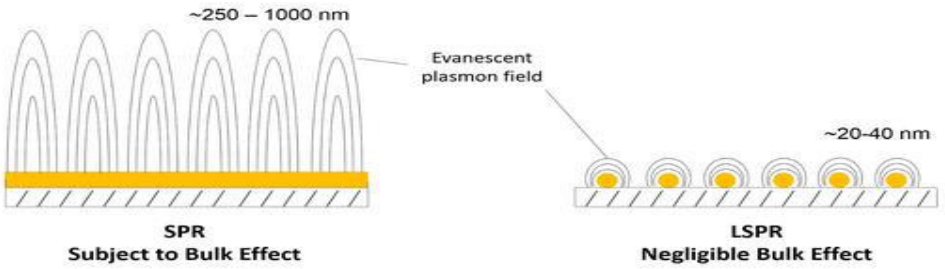

Figure 2.10 The difference between SPR and LSPR for bulk effect [6]

2.7 Drude-Sommerfield model / Free electron model

In solid-state physics, the free electron model is a simple model for the behavior of valence electrons in a crystal structure of a metallic solid. It was developed primarily by Arnold Sommerfield, who combined the classical Drude Model with quantum mechanical Fermi-Dirac statistics and hence, it is also known as the **Drude-Sommerfield Model**.

The free electron empty lattice approximation forms the basis of the band structure model known as nearly free electron model. Given its simplicity, it is surprisingly successful in explaining many experimental phenomena, especially:

- the Wiedemann–Franz law which relates electrical conductivity and thermal conductivity;
- the temperature dependence of the heat capacity;
- the shape of the electronic density of states;
- the range of binding energy values;
- electrical conductivities;
- thermal electron emission and field electron emission from bulk metals.

Similar to the Drude Model, valence electrons are assumed to be entirely separated from their ions, forming an electron gas. Similar to the properties of an ideal gas, electron-electron interactions are completely ignored. The electrostatic fields are weak in metals because of the screening effect.
The crystal lattice is not clearly taken under consideration. A quantum-mechanical explanation is given by Bloch's Theorem: an unbound electron moves in a periodic potential as a free electron in vacuum, except for the electron mass m becoming an effective mass m^* which may deviate considerably from m. It is even possible to use negative effective mass to describe conduction by electron holes. Effective masses can be derived from band structure computations. Even though the static lattice does not hamper the motion of the electrons, the electrons can be scattered by phonons and by impurities. These two determine the electrical and thermal conductivity (superconductivity requires a more refined theory than the free electron model).

According to the Pauli exclusion principle, each phase space element (Δk)3(Δx)3 can be occupied only by two electrons (one per spin quantum number). This restriction of available electron states is taken into account by Fermi–Dirac statistics (see also Fermi gas). Main predictions of the free-electron model are derived by the Sommerfeld expansion of the Fermi–Dirac occupancy for energies around the Fermi level.

Energy and Wave Function of a Free Electron

For a free particle the potential is V(R) = 0. The Schrödinger equation for such a particle, like the free electron, is:

$$-\frac{\hbar^2}{2m}\nabla^2\Psi(\mathbf{r},t) = i\hbar\frac{\partial}{\partial t}\Psi(\mathbf{r},t)$$

The wave function ψ(r,t) can be split into a solution of a time dependent and a solution of a time independent equation. The solution of the time dependent equation is:

$$\Psi(\mathbf{r},t) = \psi(\mathbf{r})e^{-i\omega t}$$

With energy,

$E = \hbar\omega$

The solution of the time independent equation is:

$$\psi_{\mathbf{k}}(\mathbf{r}) = \frac{1}{\sqrt{\Omega_r}}e^{i\mathbf{k}\cdot\mathbf{r}}$$

With a wave vector k.Ωr is the volume of space where the electron can be found. The electron has a kinetic energy:

$$E = \frac{\hbar^2 k^2}{2m}$$

The plane wave solution of this Schrödinger equation is:

$$\Psi(\mathbf{r},t) = \frac{1}{\sqrt{\Omega_r}}e^{i\mathbf{k}\cdot\mathbf{r}-i\omega t}$$

For solid state and condensed matter physics, the time independent solution ψk(r) is extremely intriguing. It is the basis of electronic band structure models that are widely used in solid-state physics for model Hamiltonians like the nearly free electron model and the tight binding model and different models that use a Muffin-tin approximation. The Eigen functions of these Hamiltonians are Bloch waves which are modulated plane waves.

3. Bimetallic nanocube-nanosphere biosensor

3.1 Analysed structure

The sphere-cube nanoparticle is placed on top of a substrate (SiO_2). The substrate and the nanoparticle are immersed in water and the entire setup is illuminated with light. We will simulate the power absorbed by the particle, the electric field coupling and the LSPR shift for different conditions and parameters. The experimental setup is shown below:

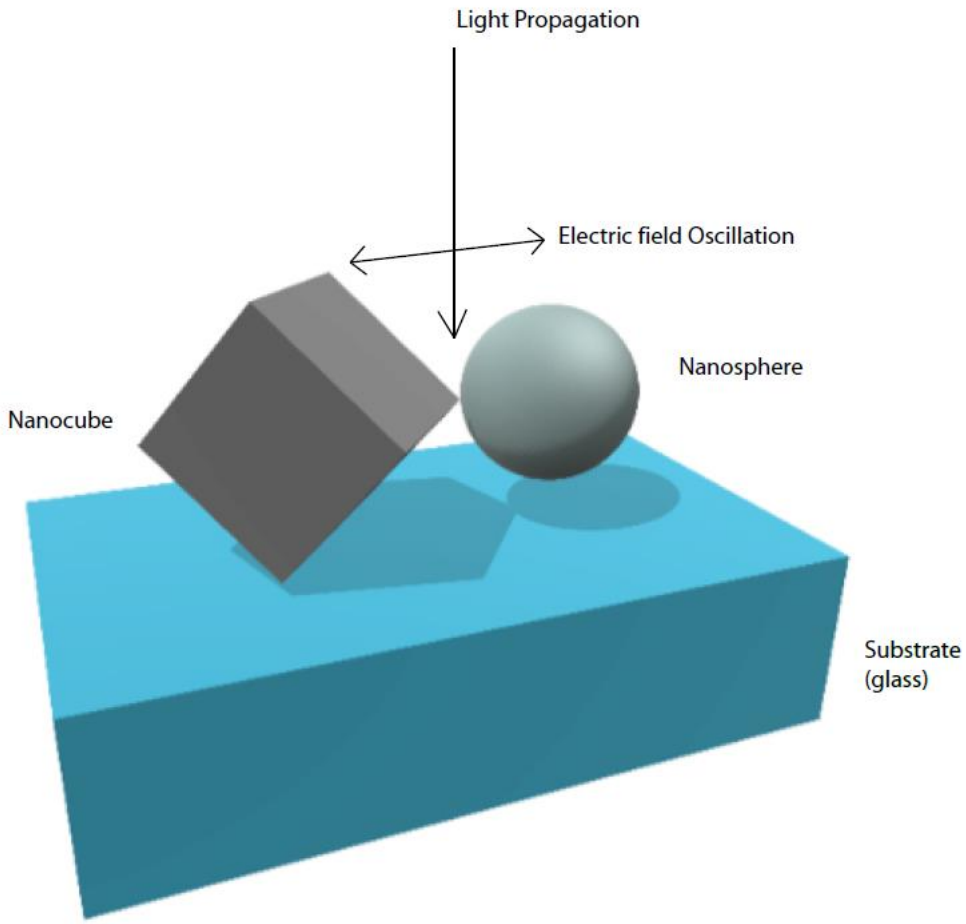

Figure 3.1 Nanocube-Nanosphere dimer

At first, the power absorption curve was observed as well as the electric field coupling for various different material combinations of gold and silver. Then after the material combination with the best power absorption and electric field graphs was selected, the gap between the nanocube and nanosphere was varied keeping everything else constant. After both the optimal material combination and gap were found, the dimensions of the nanoparticle were varied. The dimensions of the nanosphere were kept constant while changing that of the cube and then the process was repeated vice versa. For all of these processes the refractive index of the medium was chosen to be that of water.

The latter part of the research focuses on the sensitivity of the biomolecule. For a particular set of dimensions, the surrounding medium was varied by changing the refractive index, and the corresponding sensitivity curve and the LSPR Shift curve was obtained and analysed. Finally, the simulation was repeated with the other curves and analysed.

3.2 Protein as a Biomolecule

Biomolecules are any type of organic molecules, such as macromolecules or DNA, found or produced by living organisms. There are four main categories of **biomolecules** in living organisms: carbohydrates, lipids, amino acids/proteins and nucleotides. Proteins are composed of subunits called amino acids and make up the majority of **biomolecules** present in a cell. These molecules have enormous variation and are responsible for many enzymatic **functions** in the cell and play an important structural role.

The biomolecules that we have used for our thesis paper have been mentioned below along with their refractive indices for different buffer solutions [7]:

Buffer solution	Lys refractive index	FB refractive index	HSA refractive index	IgG refractive index
40 microgram/mL HEPES	1.5	1.39	1.45	1.41
80 microgram/mL HEPES	1.475	1.4	1.415	1.41
6M Urea	1.48	1.43	1.415	1.42

Table 3.1 Refractive indices of each biomolecule corresponding to each buffer solutions

3.2.1 Lysozyme (Lys)

Lysozyme is an antimicrobial enzyme also known as N-acetylmuramide glycanhydrolase. It is commonly found in tears, mucus, saliva and other secretions. Its molecular weight is 14100±500 and its shape is that of a stubbly prolate ellipsoid of rotation, with a maximum length of 90 Å and a minimum equatorial diameter of 18 Å depending on the level of hydration assumed [8].

The importance of Lysozyme is that it can act as a biomarker for Rheumatoid Arthritis [9].

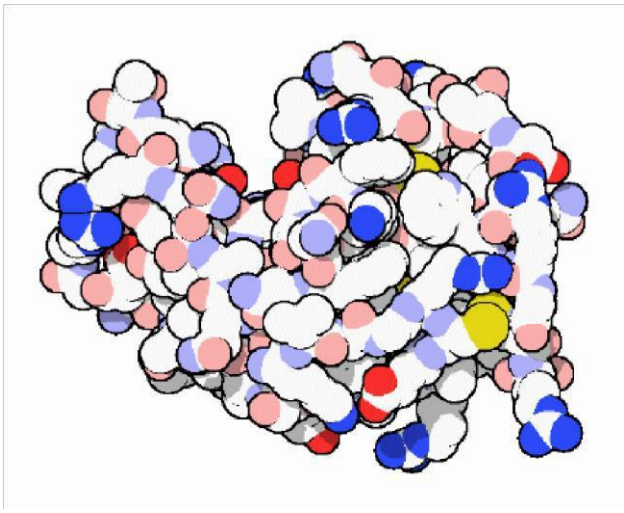

Figure 3.2 Lysozyme

3.2.2 Human Serum Albumin (HSA)

Human serum albumin is the most abundant protein found in plasma. It helps to maintain pH and osmotic pressure of the blood. The primary sequence of HSA shows that the protein is a single polypeptide with 585 residues containing 17 pairs of di-sulfide bridges and one free cysteine [10].

The importance of Human Serum Albumin is that it can act as a biomarker for Stacybotrys chartarum [11].

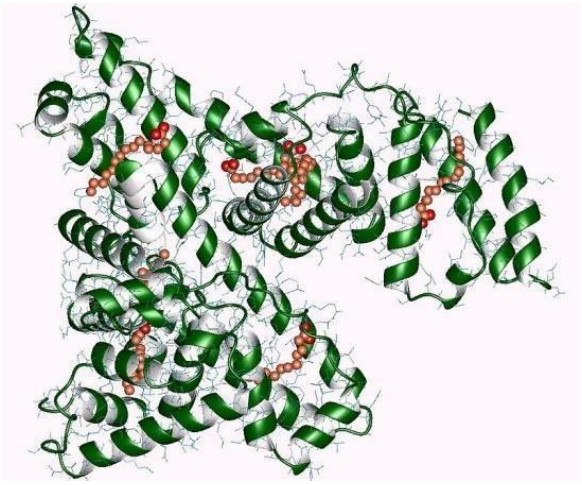

Figure 3.3 Human Serum Albumin

3.2.3 Human Fibrinogen

Fibrinogen is a glycoprotein in vertebrates that helps in the formation of blood clots. It has a molecular weight of 600000 and its shape is that of a prolate ellipsoid 700 Å long with an axial ratio of 18 [12].

Human fibrinogen can act as a stress biomarker [13].

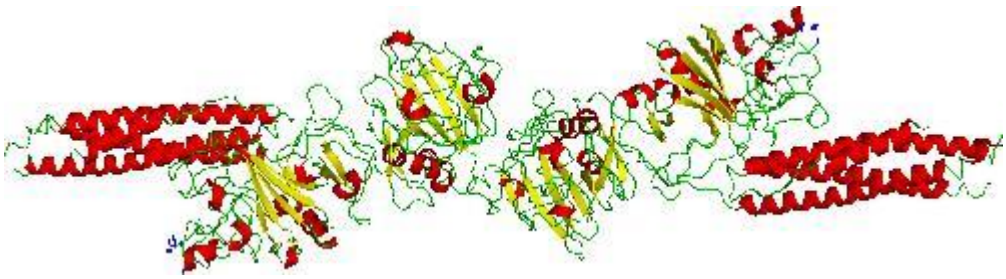

Figure 3.4 Human Fibrinogen

3.2.4 Human γ-immunoglobulin (IgG)

The four human IgG subclasses are bilaterally symmetric glycoproteins that are composed of two heavy (M_r Ca. 50000) and two light (M_r Ca. 25 000) polypeptide chains, which are held together by noncovalent forces and covalent interchain disulfide bridges [14].

IgG is a good indicator of cardiomyopathy [15].

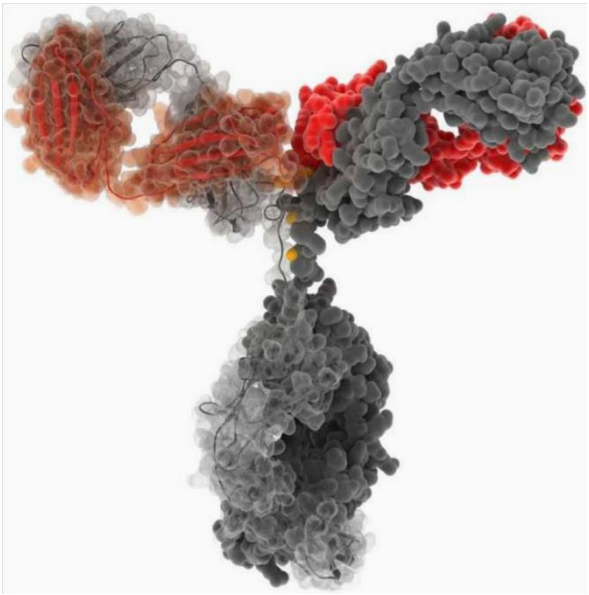

Figure 3.5 Human Immunoglobulin G

4. FDTD simulation

4.1 Introduction

Our main target is to create a nanocube and a nanosphere non uniform structure. The nanoparticles are placed on Silicon Dioxide (SiO_2) substrate. The setup was illuminated with light and the power absorption curve of the nanoparticle observed. Also the electric field coupling of the Ordinary Plasmon Resonance was analysed.

4.2 About Finite-Difference Time-Domain (FDTD) solutions

FDTD solutions is a high performance 3D FDTD (Finite-Difference-Time-Domain)-method Maxwell solver for designing, analysing and optimization of Nano photonic devices, its process and materials are developed by the Lumerical company. Its applications include Solar cells, grapheme, and metamaterials and many others [17]. We used it for the simulation of localised surface plasmon resonance of nanocubes and nanospheres.

4.2.1 General

The directory: “Simulation > Region > General”.

We first set the value of the “background index” to 1.33 to match the refractive index of water. This process is repeated for many different background indexes and the different responses taken into account. Next we set the “Simulation time”. The larger the simulation time, the larger the file size and more likely that the program will slow down. But a very small value does not get us the desired results either therefore, we select an optimum value of 300 femtoseconds.

4.2.2 Geometry

Going into the “Geometry” section located right next to “General” there are six options: x (nm), y (nm), z (nm), x span (nm), y span (nm) and z span (nm). We set x span to 400 nm, y span to 400 nm and z span to 100 nm.

4.2.3 Boundary conditions

Inside the “Boundary Conditions” section there are six options called “x min bc”, “x max bc”, “y min bc”, “y max bc”, “z min bc” and “z max bc”. All are set to PML.

PML (Perfectly Matched Layers) absorbing boundary conditions are impedance matched to the simulation region and its materials [16]. This allows them to absorb light waves (both

propagating and evanescent) with minimal reflection. An ideal PML boundary produces zero reflections, however, in practice there are always small reflections due to the decentralisation of the underlying PML equations. Furthermore, as a consequence of using finite difference approximations to decentralise the PML equations, there are some chance of producing numerical instabilities.

4.3 Mesh analysis

We first click on “Simulation” then go to “Mesh”. Mesh grid settings involve a compromise between accuracy and file size. The smaller the size of each cell the more measurements that are taken, hence, we are given a higher resolution image of the processes taking place. But as more measurements are taken, the file size increase and if it is comparable to the RAM size, the computer hangs. Even if it does not hang, the simulation time may greatly increase. Since the computer used has a RAM size of 16 GB, the grid size is selected in a way such that the file size is well below 16 GB.

The size of the whole mesh can be changed by altering the x-span, y-span and z-span which can be accessed by right-clicking the mesh then clicking on “Edit Properties”. The mesh is made to completely cover the objects being analysed by having dimensions slightly larger. The position must also be selected as such, it can be done by manipulating the x, y or z values in “Edit Properties”.

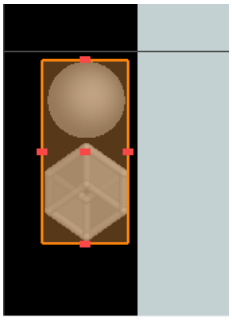

Figure 4.1 Mesh covering the nanoparticles

4.4 Power Absorption (Advanced)

The directory: “Analysis”>”Optical Power”>”Power Absorbed (Advanced)”.

The advanced version of power absorption calculates the power absorbed per unit volume (Pabs) due to material absorption but unlike the simple version it minimizes interpolation errors due to discontinuities in the electric field near the interface [18]. After simulation the absorption profile can be viewed as graph.

4.5 Monitor

The directory: “Monitor > Frequency – domain field and power”.

“Frequency – domain field and power” is selected because this type of monitor ‘snaps’ to the nearest mesh cell reducing the amount of interpolation required, thus increasing accuracy.

The dimensions of the monitor are selected in a way that encompasses the mesh and the objects within it. We tick “override global monitor settings” so that we can enter the desired frequency points. Under “Geometry”, the Monitor Type is set to 2D X-normal (along the direction of the thickness of the substrate) which auto-sets the x-span to zero.

The monitor gives us the electric and magnetic field profiles. This can be done either for a range of wavelengths or a particular wavelength.

4.6 Material modelling

After installing and opening the FDTD solutions software, four windows opened each introducing its own perspective. The upper left window indicate XY view while the upper right window indicate the 3D view of the particle. The lower left window indicates the XZ view and lower right window indicates the YZ view.

Since we have decided to use nanoparticles, initially we went to “Settings” and selected nanometres for all length units. Then we insert the nanoparticle structure according to direction: Components> Ellipsoid>Coated Sphere & Cube. We insert the Coated Sphere and cube to simulate two metals with four combination, i.e. gold and silver.

Moving on, we went to the “Coated Sphere” option and selected “edit object” option in order to set the dimensions of the nanoparticle. It opens a window where we can change the material, radius, rotation, length etc. We selected the initial radius of coated sphere to be 12.5 nm and it was varied from radius 7.5 nm to 22.5 nm. The same thing was done for the cube as was done for the coated sphere, the length for each cube was selected to be 20 nm initially while varying from 17.1 nm to 34.6 nm. Then later we changed the material for sphere and cube. Because there are two nanostructures with two kinds of materials we have four combinations of materials, i.e. gold-gold, gold-silver, silver-gold, and silver-silver.

4.7 Substrate formation:

The structure on top of which the nanosphere-nanocube is placed, is the substrate. It can be constructed of numerous different materials. In our research we used “SiO_2 (Glass)-Palik”. SiO_2 has some advantages which influenced our selection. Firstly, it is affordable and also

silicon spontaneously creates a layer of SiO_2 on its surface by responding with Oxygen present in air.

For applying the substrate to our structure, we went to the "Object Library" located to the right of the four windows. Then from the category "Extruded Polygons" we selected "Quadrilateral". We changed the "Geometry" of the "Quadrilateral". Six options are there: x (nm), x span (nm), y (nm), y span (nm), z (nm), and z span nm. We set the following values,

X span= 80 nm

Y span= 270.685 nm

Z span= 100.265 nm

Finally, the substrate was rotated in the x direction because the thickness was in x direction.

The refractive index of Silicon Dioxide is 1.46.

Benefit of Silicon Dioxide:

1) Thickness control optimum
2) High specific heat capacity
3) Die attach easily reworked
4) Cheap

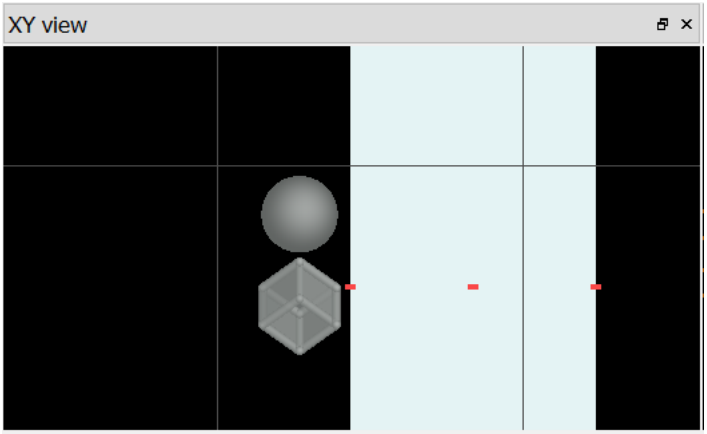

Figure 4.2 Nanoparticles on top of substrate

4.8 Source

To install the light source in our structure, the direction for editing the setup is “Source>Total Field Scattered Field (TFSF)”. Our target is adding a light to our existing components. As it is TFSF, so the light will fall on the structure equally. Now object editing is done.
Progressing, the “General” setting is changed with the injection axis set in the x direction (along the thickness direction). The value of amplitude is fixed at 5 for easy understanding.

Once again we changed the “Geometry” of the quadrilateral. Six options are there: x (nm), x span (nm), y (nm), y span (nm), z (nm), and z span nm. We fixed the value of x, y and z at 0 and set the value of x span (nm), y span (nm) and z span (nm) according to our preference. It is not needed to choose too large a value. We fix the value in such a way that the entire nanoparticle can be covered fully.

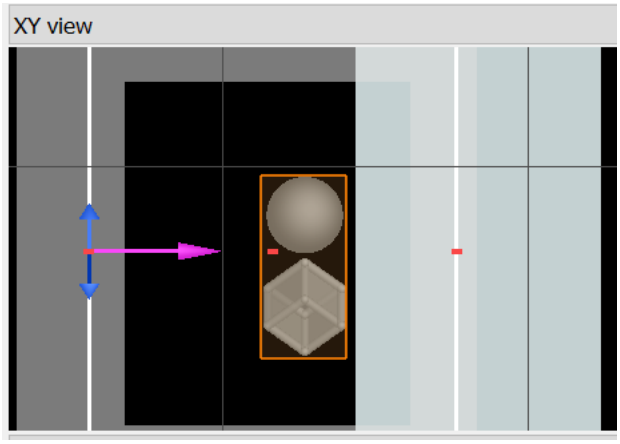

Figure 4.3 Light source aimed at nanoparticles. The purple arrow is the direction of propagation and the blue arrows are the direction of oscillation of the electric field component.

5. Simulation and result analysis

5.1 Introduction

After all the settings in the FDTD solutions software was taken care of, we started simulation. The nanocube-nanosphere was chosen as it is a fairly uncommon structure and also because the cube has a sharp tip that might help with the excitation. For each simulation, a power absorption (Pabs) graph and an electric field coupling graph were the results.

Our result analysis has been classified into five parts:

- Materials

    1. Au-Au
    2. Au-Ag
    3. Ag-Au
    4. Ag-Ag

- Gap change between nanosphere and nanocube.
    1. 1 nm
    2. 2 nm
    3. 5 nm
    4. 8 nm
    5. 10 nm
- Physical dimension

    1. Change in side length of Cube
    2. Change in diameter of Sphere

- Sensitivity analysis

- Sensitivity analysis for biomolecule proteins

5.2 Materials

Four combinations of two different materials were simulated while keeping the other factors constant. They were, Au-Au, Au-Ag, Ag-Au, and Ag-Ag. For all of these, the cubes have sides of length 20 nm (diagonal 35 nm) and the spheres have radius 12.5 nm (diameter 25 nm). Since we were unsure about which wavelength at which we might get peaks, the first simulation had a wavelength range of 100 nm-900 nm. The number of frequency points at this wavelength range was set to 1600 because we wanted to take two readings for every 1 nm. This number was changed later to cater for different wavelength ranges. The mesh was set at 1 nm and the refractive index of the background at 1.33.

5.2.1 Au-Au (NC-Au, NS-Au)

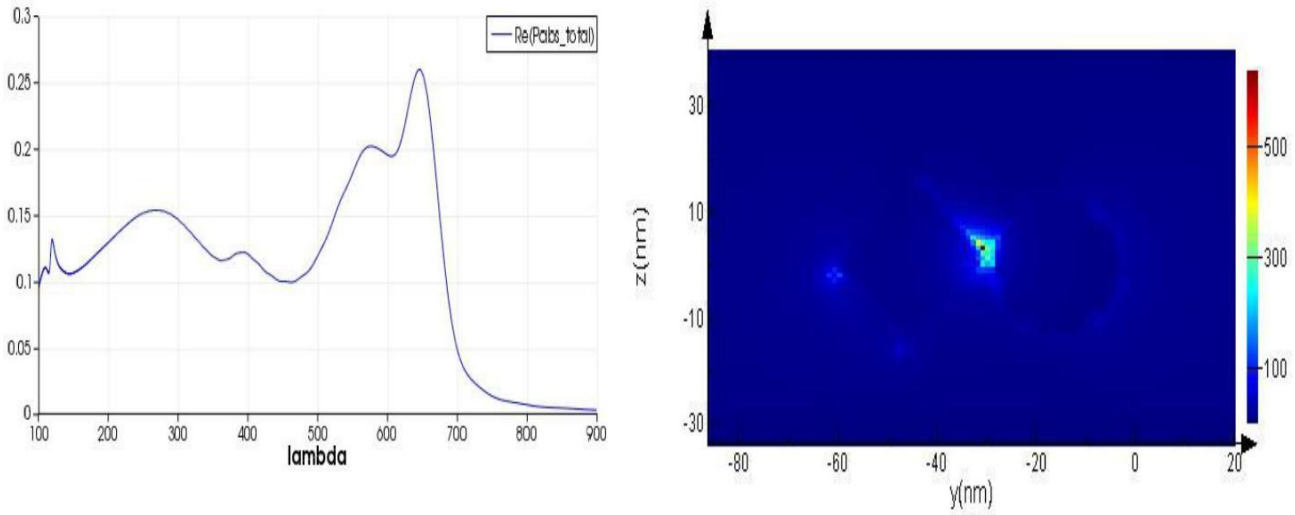

(a) (b)

Figure 5.1 (a) Pabs of Au-Au (b) Electric field coupling of Au-Au

As shown above, we observe multiple peaks when simulating for 100 nm-900 nm but most of these are not very sharp and are also too close together and thus not very discernible. But there is one fairly noticeable peak between 600 nm and 750 nm thus we repeatedly simulate focusing on that range. The electric field coupling diagram shows fairly low scattering with the vast majority of the coupling occurring in the gap between the sphere and the cube with the values mostly being around 300 but some values around 400 nearer to the cube edge.

Wavelength 610 nm-690 nm

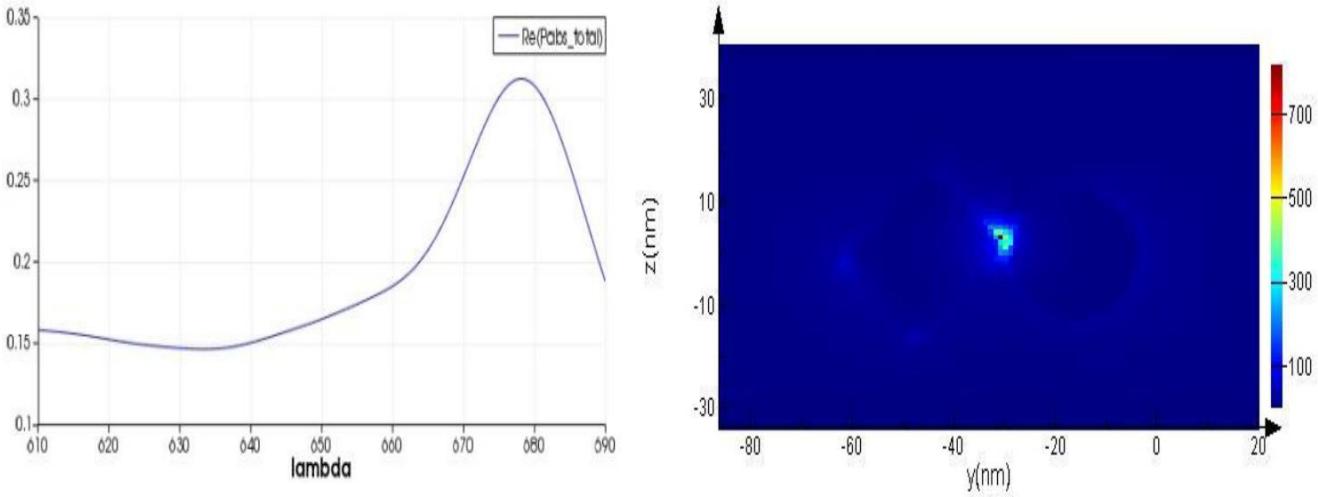

(a) (b)

Figure 5.2 (a) Pabs of Au-Au (610 nm-690 nm) (b) Electric Field Coupling of Au-Au

Here we did not get multiple peaks, only one very clear one at 678.093 nm, therefore this focused range is better for detection as multiple peaks are difficult to differentiate. The values for E-field coupling are higher with slightly less scattering.

Wavelength 650 nm-750 nm

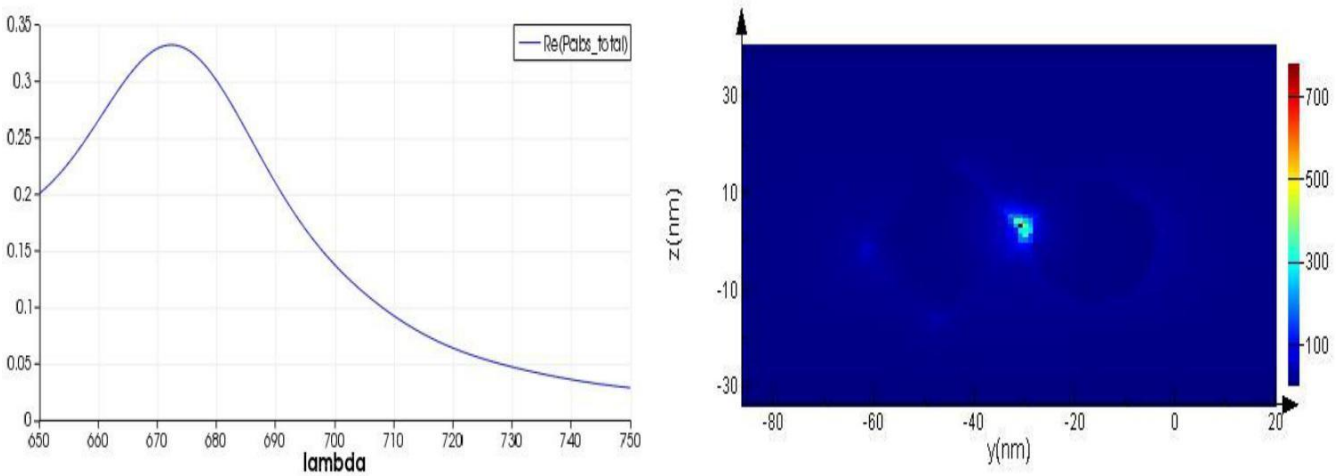

(a) (b)

Figure 5.3 (a) Pabs of Au-Au (650 nm-750 nm) (b) Electric field coupling of Au-Au

For this range too we observe a clear single peak but at a slightly different wavelength (672.24 nm). The E-field coupling diagram is similar to that before.

5.2.2 Au-Ag (NC-Au, NS-Ag)

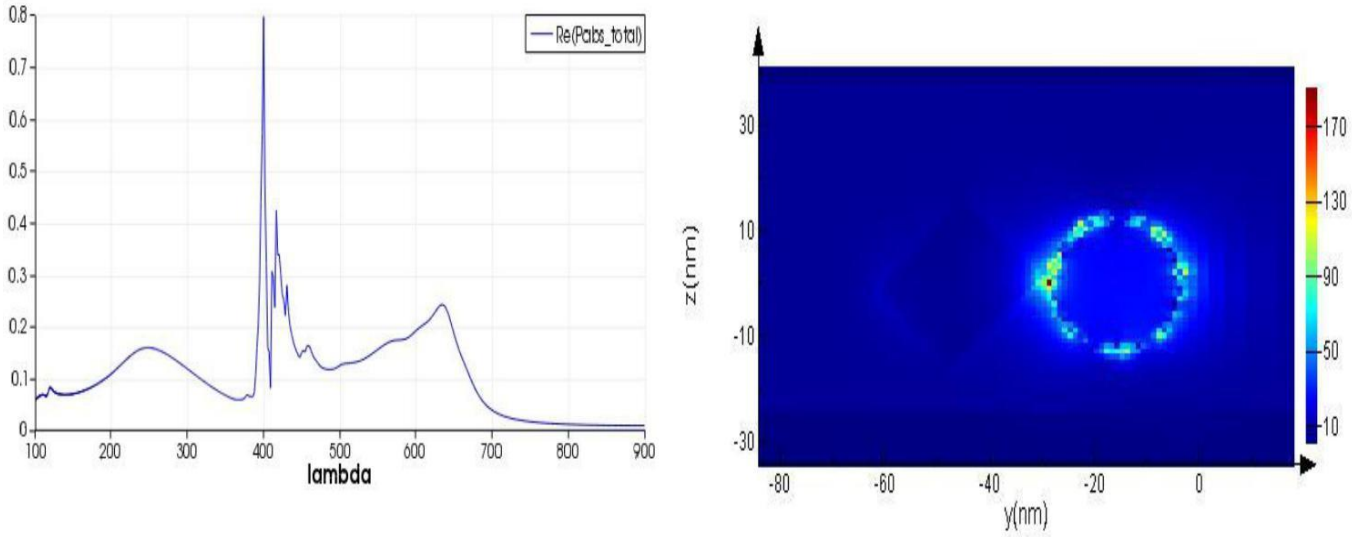

(a) (b)

Figure 5.4 (a) Pabs of Au-Ag (100 nm-900 nm) (b) Electric field coupling of Au-Ag

For 100 nm-900 nm there are multiple peaks many of which grouped very close together and some a bit separate. The E-field coupling for the peak wavelength is not so favourable, as the values are too low (maximum around 170) and there is a tremendous amount of scattering, mostly around the sphere.

We focus on 375 nm-425 nm as the highest peak occurs in that vicinity and also on 500 nm-600 nm.

Wavelength 375 nm-400 nm

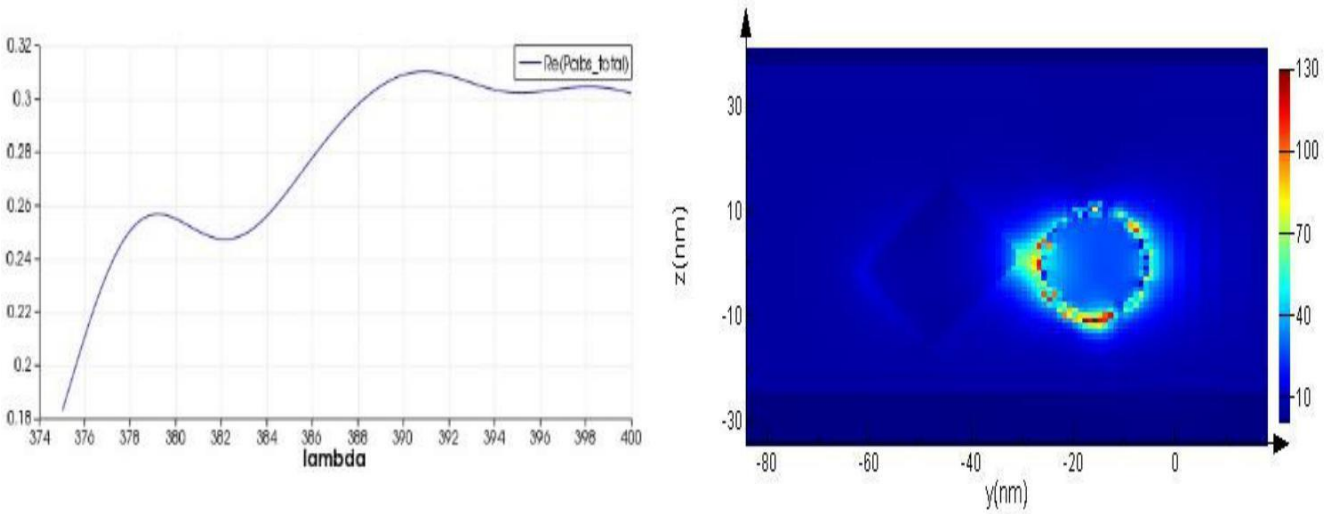

(a) (b)

Figure 5.5 (a) Pabs of Au-Ag (375 nm-400 nm) (b) Electric field coupling of Au-Ag

Wavelength 400 nm-425 nm

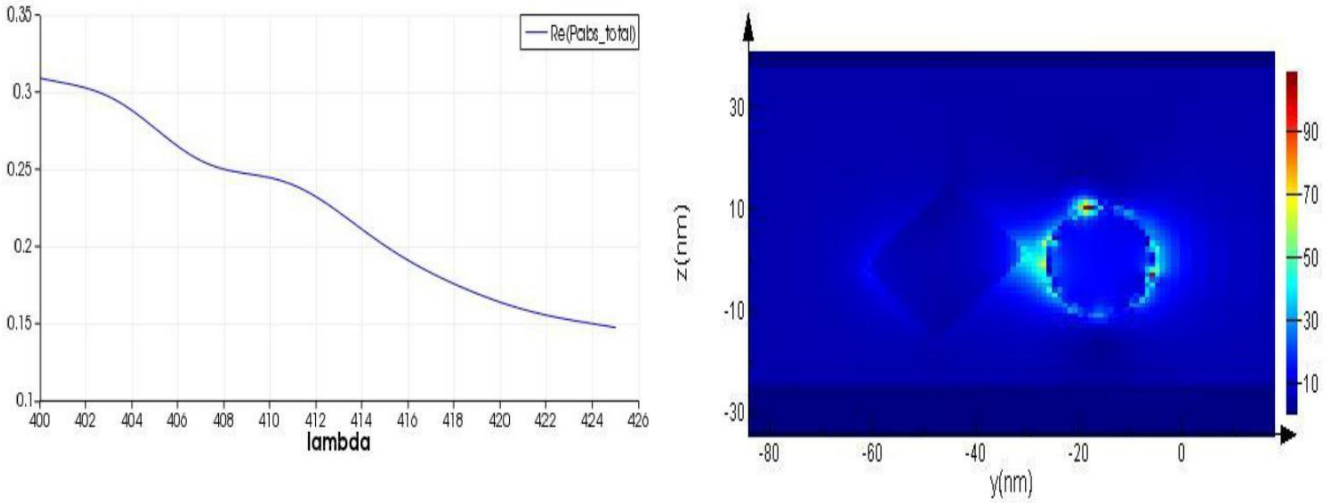

(a) (b)

Figure 5.6 (a) Pabs of Au-Ag (400 nm-425 nm) (b) Electric field coupling of Au-Ag

We do not get anymore multi-peaks like previously (Fig: 1.4 a) but at the same time there are no sharp rising points at all, also the scattering has risen and the E-field values have dropped.

Wavelength 500 nm-600 nm

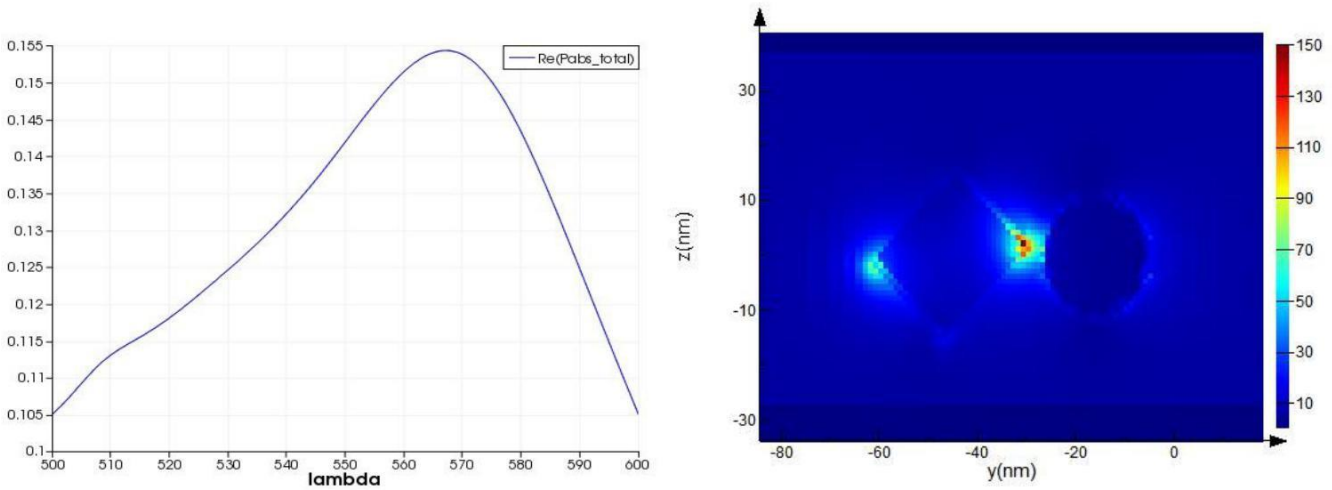

(a) (b)

Figure 5.7 (a) Pabs of Au-Ag (500 nm-600 nm) (b) Electric field coupling of Au-Ag

For this range, we obtain a single properly differentiated peak at wavelength 567.26 nm. The E-field graph, although far superior to its previous ones, still has some scattering i.e. the coupling is not restricted to the gap between cube and sphere and the values are fairly low.

5.2.3 Ag-Au (NC-Ag, NS-Au)

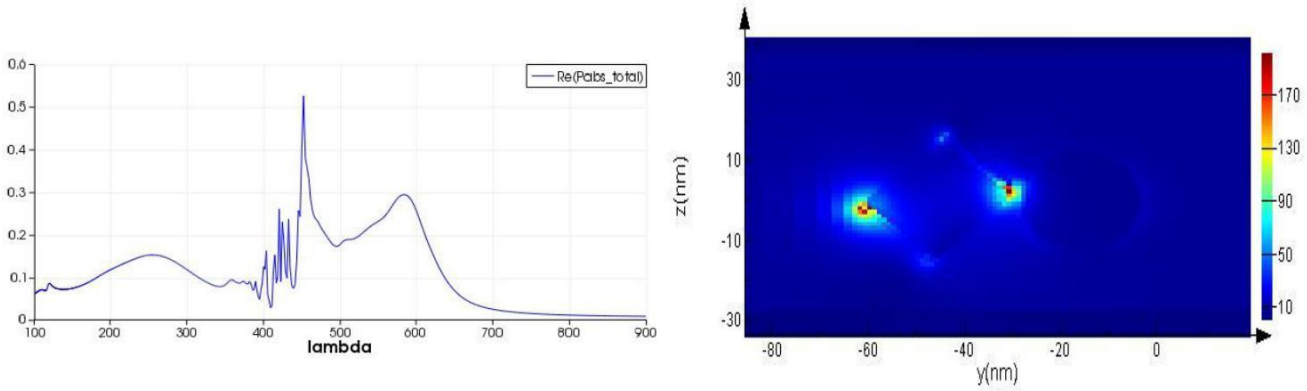

(a) (b)

Figure 5.8 (a) Pabs of Ag-Au (100 nm-900 nm) (b) Electric field coupling of Ag-Au

There are many extremely close together peaks around 400 nm-450 nm, one very sharp peak around 450 nm and another less sharp but still distinguishable peak between 575 nm-600nm. E-field coupling takes place both at the gap between the cube and sphere and also at the opposite edge of the cube. Values mostly around 90 but close to the cube edges it is around 150.

Wavelength 435 nm-485 nm

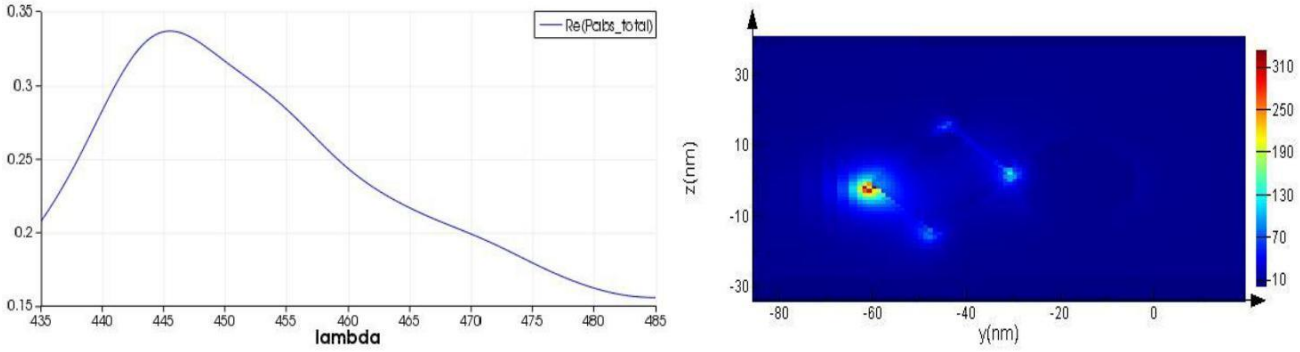

(a) (b)

Figure 5.9 (a) Pabs of Ag-Au (435 nm-485 nm) (b) Electric field coupling of Ag-Au

A clear peak at 445.383 nm. The E-field coupling takes place almost entirely at the edges of the cube with the most at the opposite edge of the cube-sphere gap, second-most at the gap and even less at the other edges. The E-field values have gone up somewhat with mostly being around 130 but can be near 310 at the opposite edge of the gap.

Wavelength 600 nm-640 nm

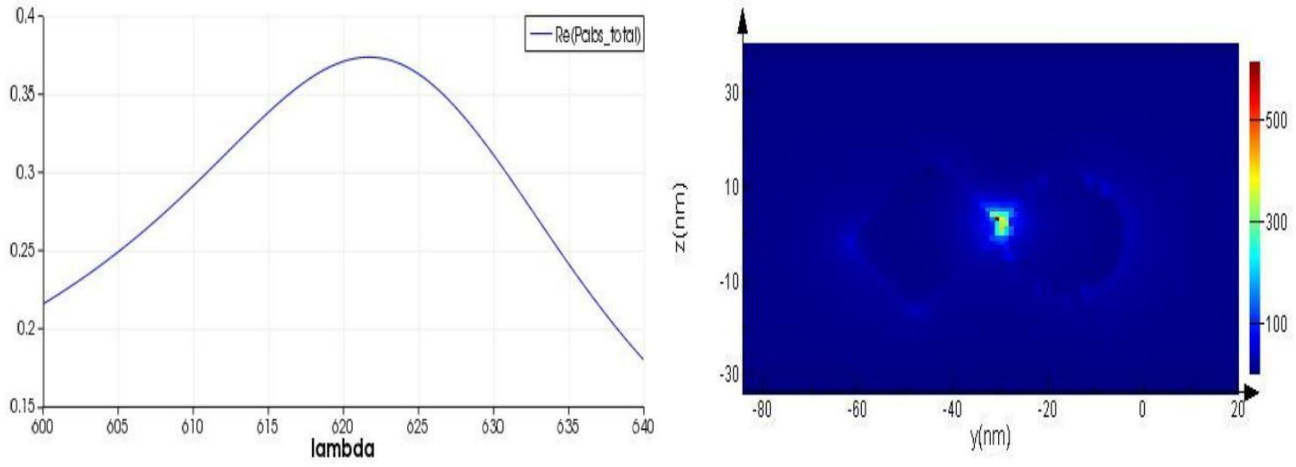

(a) (b)

Figure 5.10 (a) Pabs of Ag-Au (600 nm-640 nm) (b) Electric field coupling of Ag-Au

A single Pabs peak at 621.752 nm. The E-field graph, similar to before, has low scattering with most coupling in the gap but this time the values are higher. Most of the values are around 300, nearer to the centre and 500 nearer to the cube.

5.2.4 Ag-Ag (NC-Ag, NS-Ag)

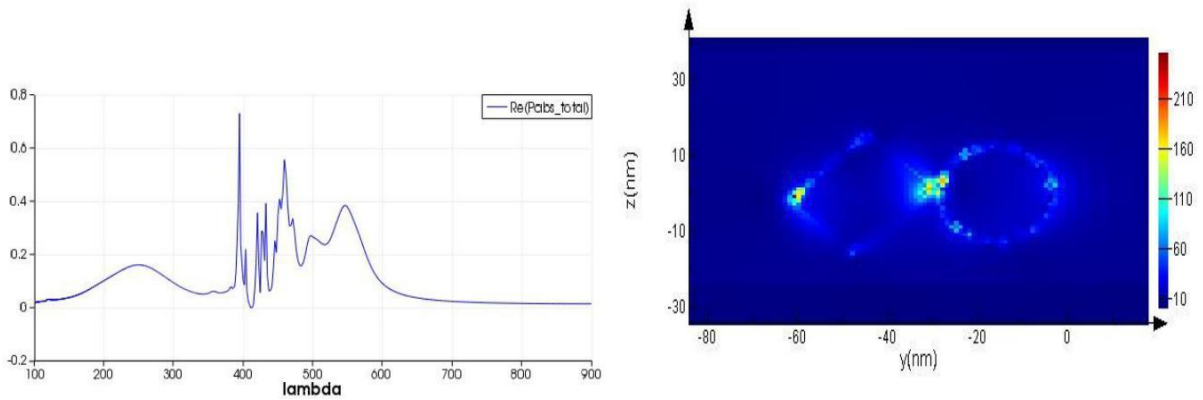

(a) (b)

Figure 5.11 (a) Pabs of Ag-Ag (100 nm-900 nm) (b) Electric field coupling of Ag-Ag

From the Pabs graph we can see lots of sharp, closely-packed multi-peaks between 400 nm and 500 nm and one discernable but less sharp peak between 500 nm and 600 nm. The E-field graph shows a fair amount of scattering with only a slight majority of the coupling in the gap with the values there mostly around 160.

Wavelength 375 nm-400 nm

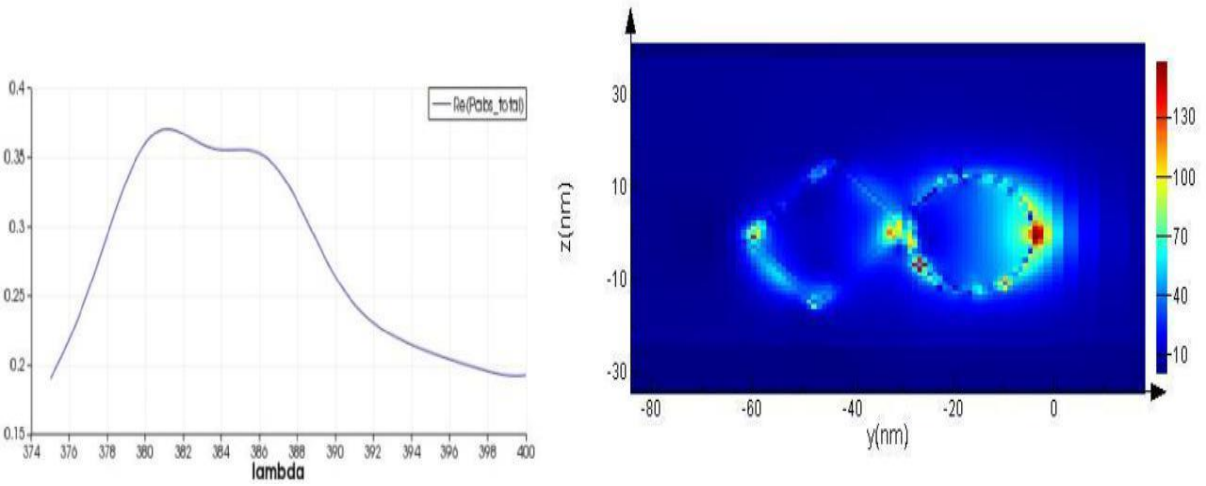

(a) (b)

Figure 5.12 (a) Pabs of Ag-Ag (375 nm-400 nm) (b) Electric field coupling Ag-Ag

No distinguished peak from the Pabs graph. Tremendous scattering seen from the E-field graph with a slight majority of the coupling occurring at the end of the sphere opposite to the gap. Values are mostly between 100 and 130.

Wavelength 450 nm-480 nm

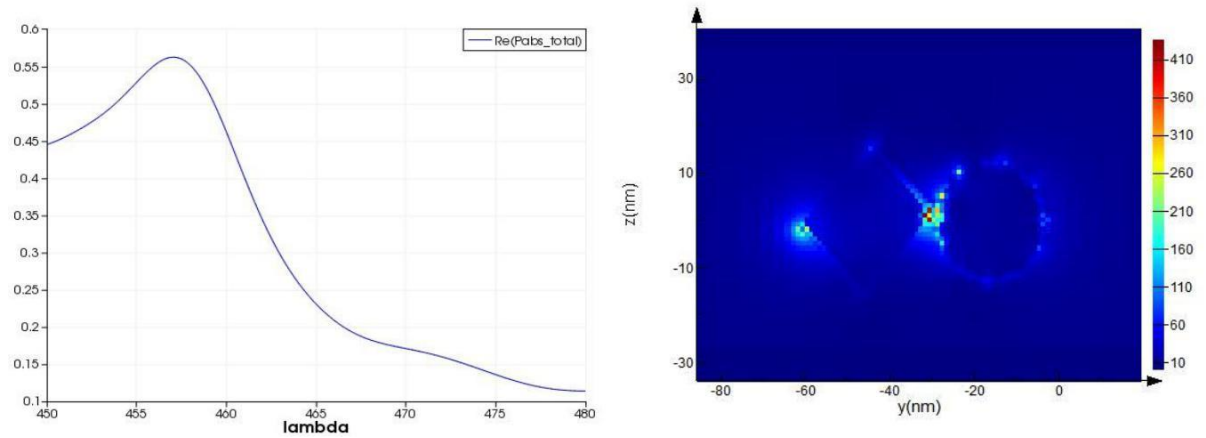

(a) (b)

Figure 5. 13 (a) Pabs of Ag-Ag (450 nm-480 nm) (b) Electric field coupling of Ag-Ag

Pabs graph shows a somewhat discernable peak between 455 nm and 460 nm. The E-field graph shows most of the coupling being in the gap with values mostly around 200 but near the middle it is 260 and 400 near the cube. But there is some scattering-taking place at the opposite end of the cube.

Wavelength 530 nm-570 nm

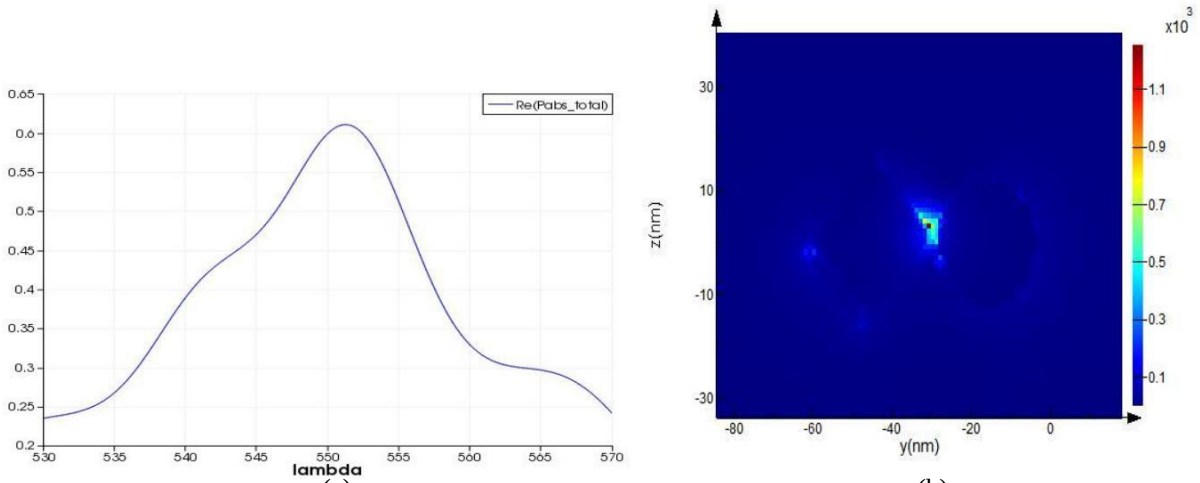

(a) (b)

Figure 5.14 (a) Pabs of Ag-Ag (530 nm-570 nm) (b) Electric field coupling of Ag-Ag

The E-field graph shows minimal scattering with almost the entire coupling in the gap and the values are much higher than before with most of it being around 500 but close to the cube it rises to above 800 and even around 1000.

Summary

When we compare the material combinations we can see that the gold-gold total Pabs graph has few very sharp peaks but they are well spaced and some are quite easy to make out. The gold-silver, silver-gold and silver-silver total Pabs graphs on the other hand, have multiple very sharp peaks very close together and a few smooth ones far away. However, when the focus is on smaller wavelength ranges there are some sharper peaks for gold-silver, silver-gold and silver-silver.

The E-field graphs in general have the lowest scattering for gold-gold, second-lowest for silver-gold while silver-silver and gold-silver have similarly high scattering. But for the wavelength range of 530 nm-570 nm silver-silver gives us the highest E-field value of all with very little scattering. Thus, the silver-silver combination is used for the rest of the analysis.

5.3 Gap change

A silver-silver combination was selected where the nanosphere has a diameter of 25 nm and the nanocube has a side length 20 nm. Keeping all the other conditions constant the gap length between them was varied and the corresponding power absorption (Pabs) curves were

taken into account and the first order points (wavelengths at which we get peaks) from those curves were recorded for a wavelength range of 500 nm-600 nm.

Gap length (nm)	First Order Points (nm)
1	547.970
2	543.179
5	519.611
8	510.573
10	510.051

Table 5.1 Gap length and First Order Points

Graphical Representation

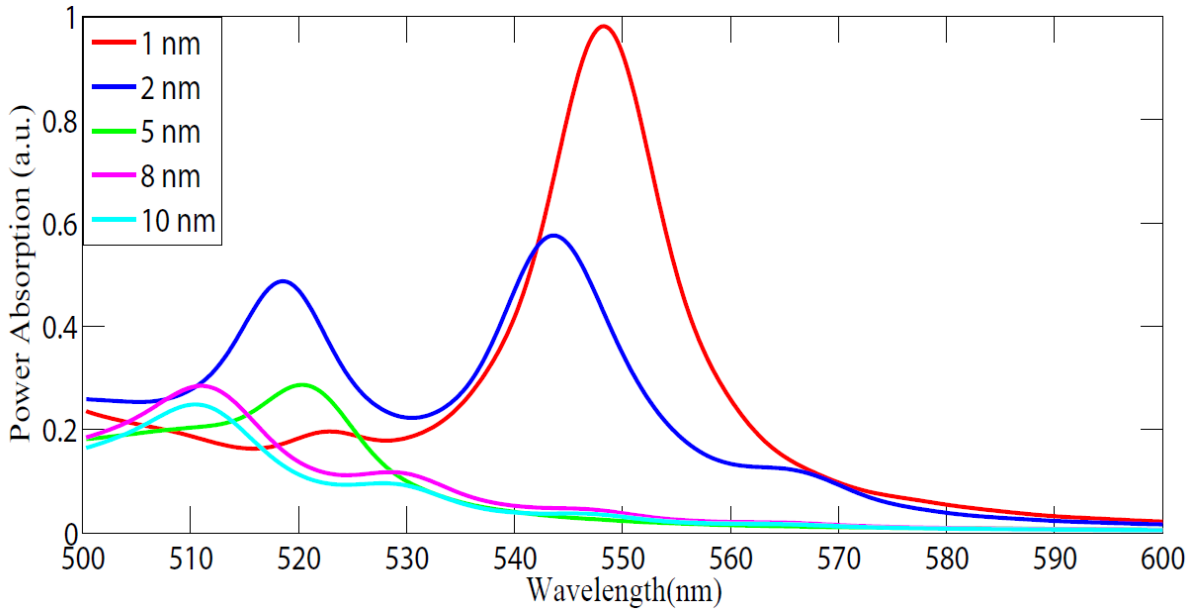

Figure 5.15 Power Absorption vs Wavelength

As we can see from Fig 5.15, for 1 nm, the graph is sharp and very easily discernible with only one single high value peak whereas for 2 nm there are two peaks close to each other with lower values. For 5, 8 and 10 nm the peaks have much lower values and are much less sharp.

So clearly, a 1 nm gap between nanocube and nanosphere has provided the best results and was thus used for the rest of the analysis.

5.4 Physical dimension

Taking the silver-silver combination, we first keep the nanosphere radius constant at 12.5 nm while changing the nanocube side length and observing the Pabs and E-field graph for each combination. We then keep the cube side length constant and change the sphere radius and repeat the process.

In the previous section we got the Pabs graph below for silver-silver for 100 nm-900 nm. As we can see the clear peak is between 500 nm and 600 nm. Since for this section we want to see how the peaks shift with size change and focus only on the peaks, we decide that the wavelength range to be 500 nm to 600nm.

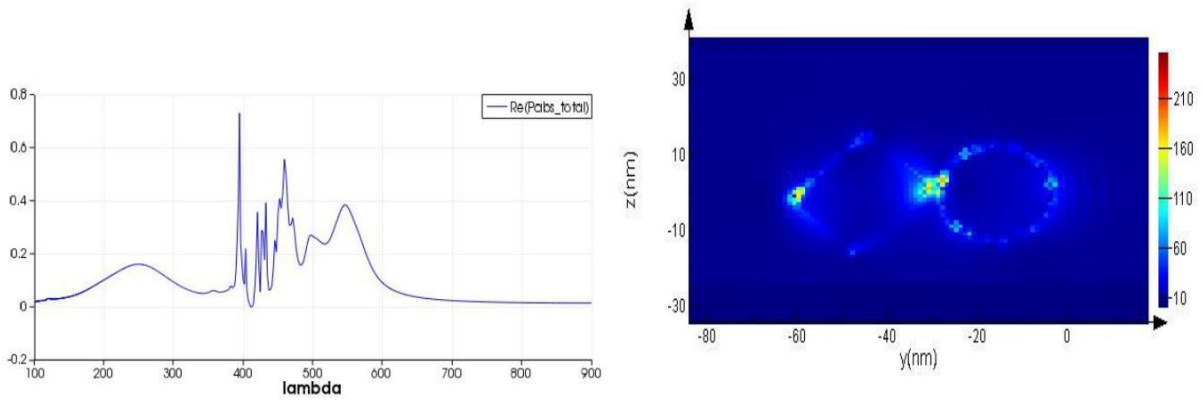

Figure 5.16 (a) Power Absorption (100 nm-900 nm) (b) E-field graph

5.4.1 Change of length of cube

The sphere radius was kept constant at 12.5 nm (diameter 25). The cube side length is changed from 17.1(diameter 30) nm to 34.6 nm (diameter 60) at diameter 10 nm intervals. For all the simulations the number of frequency points was kept at 200, the refractive index of the medium at 1.33 and the mesh values at 1 nm. The first order points (wavelength at which we get the peak point of a Pabs curve is called the first order point) were recorded for each combination.

Table of Result:

NC-NS length (nm)	First Order Points (nm)
NC-17.1,NS-12.5	564.806
NC-23.1,NS-12.5	562.677
NC-28.9,NS-12.5	553.29
NC-34.6,NS-12.5	575.581

Table 5.2 Changing nanocube with constant nanosphere and corresponding First Order Points

Graphical Representation

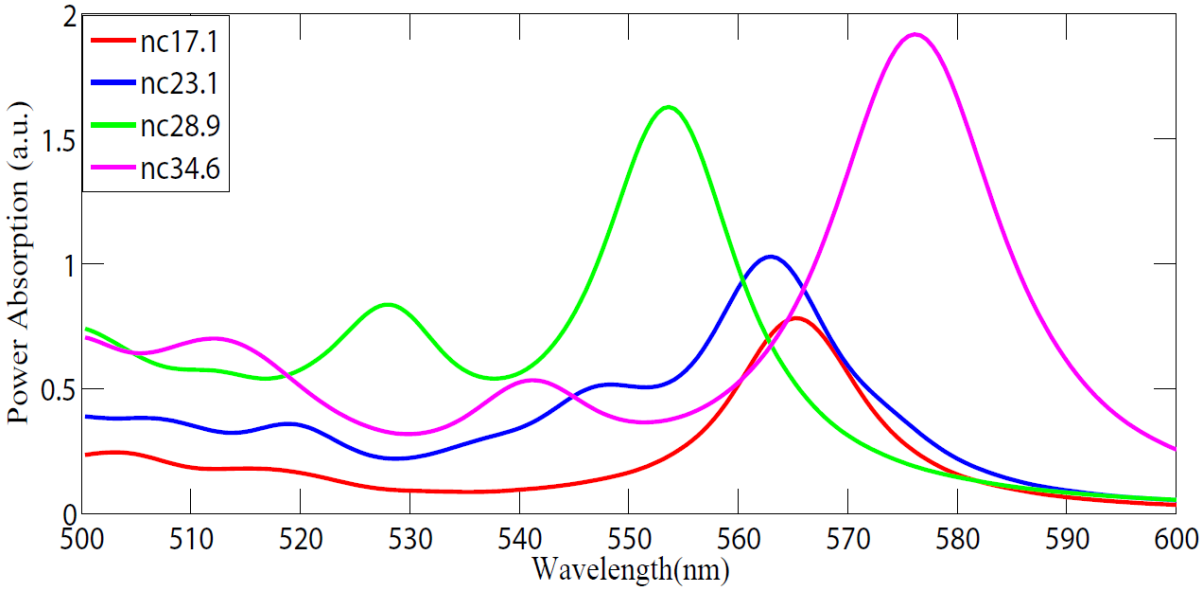

Figure 5.17 Power Absorption curve of change of length of cube

The wavelength corresponding to the maximum point for each curve represents the first order values. As the size of the cube increases, the power absorption values also increase. The values of the first order points go down as the side length is increased from 17.1 nm to 28.9 nm but then goes up as side length is increased from 28.9nm to 34.6nm. Another observation is that the curves corresponding to the larger cubes have more pronounced as well as a higher number of extra peaks.

For each of the first order points electric field coupling has been observed. In Fig 5.18 and 5.19 the E-field graphs for the smallest and largest cube respectively has been shown.

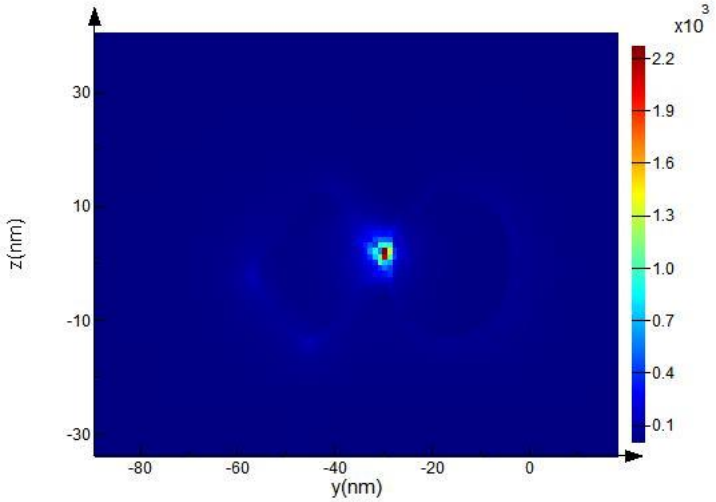

Figure 5.18 NC-17.1 nm, NS-12.5 nm

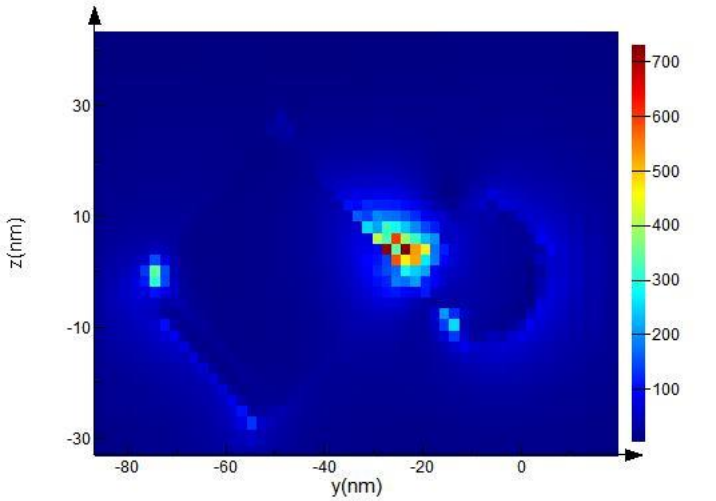

Figure 5.19 NC-34.6 nm, NS-12.5 nm

The E-field coupling value is much lower for the combination with the larger cube and there is also some more scattering at the end of the cube opposite to that of the gap.

5.4.2 Change of radius of sphere

The cube each length is kept constant at 20 nm (diameter 35 nm) while the sphere radius is changed from radius 7.5 nm (diameter15 nm) to radius 22.5 nm (diameter 45 nm) at diameter 10 nm intervals. For all the simulations the number of frequency points is kept at 200, the refractive index of the medium at 1.33 and the mesh values at 1 nm. The first order points

(wavelengths at which we get peak point of Pabs are called first order points) are recorded for each combination.

Table of Result:

NC-NS radius/nm	First order/nm
NC-20,NS-7.5	539.02
NC-20,NS-12.5	547.97
NC-20,NS-17.5	583.497
NC-20,NS-22.5	590.999

Table 5.3 Constant nanocube with changing nanosphere and corresponding First Order Points

Graphical Representation

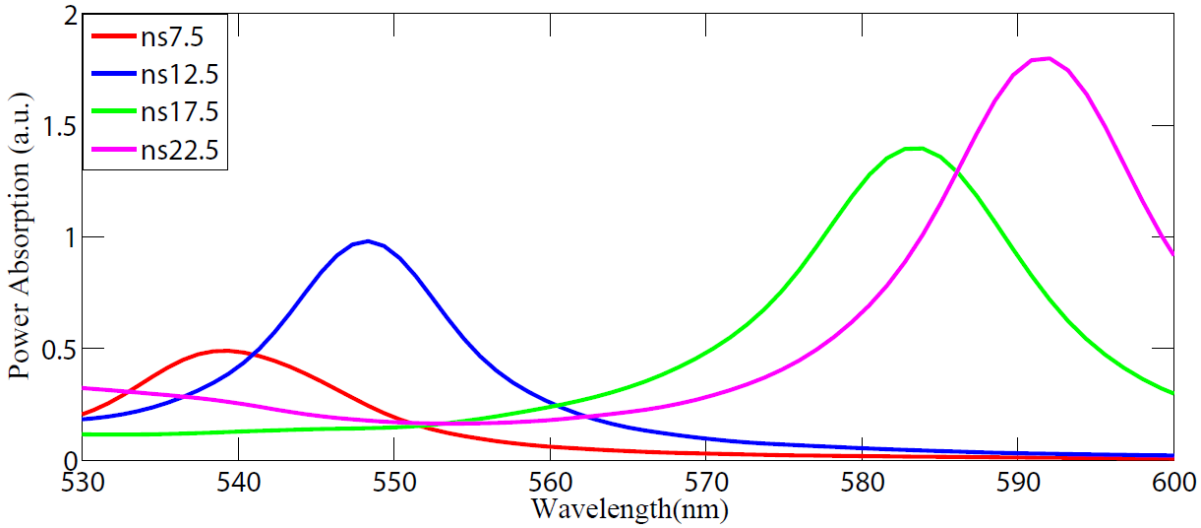

Figure 5.20 Power Absorption curve of change of radius of sphere

As sphere size increases the value of the P-absorption peaks increases and also the value of the first order points increases.

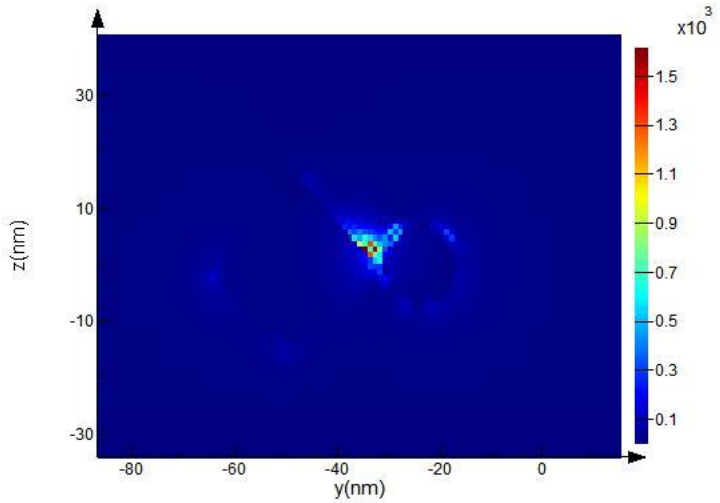

Figure 5.21 NC-20 nm, NS-7.5 nm

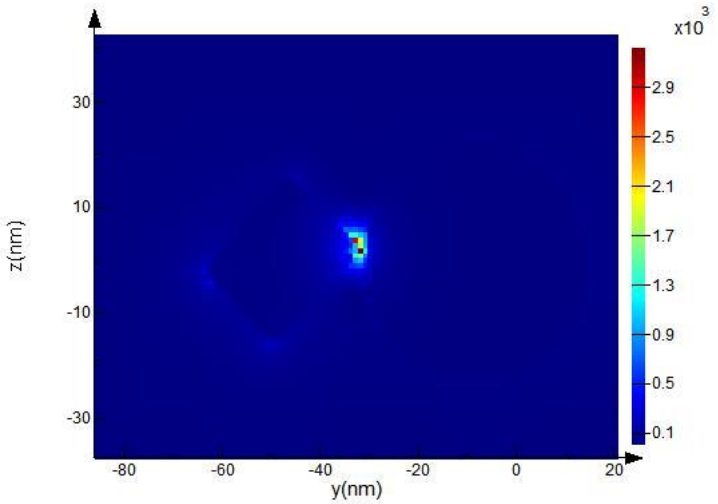

Figure 5.22 NC-20 nm, NS-22.5 nm

Looking at figures 5.21 and 5.22 we can see that while the radius of the sphere is increased from 7.5 nm to 22.5 nm, the maximum value of electric field coupling increases considerably while there is also a significant decrease in scattering especially around the sphere.

5.4 Sensitivity analysis

Here the main objective of this part of the research is to understand the sensitivity of first order points of initial structure (NC-20, NS-12.5) .The source wavelength range is 500 nm to 600 nm and the number of frequency points is 500. Here surrounding medium is at first water and then changed to different refractive indexes and the first order points recorded below.

Refractive Index, n	First Order Points/nm
1.36	556.92
1.39	565.974
1.42	574.885
1.45	584.081
1.47	590.067
1.5	598.8

Table 5.4 First Order Points vs Refractive Index

Graphical Representation of Sensitivity:

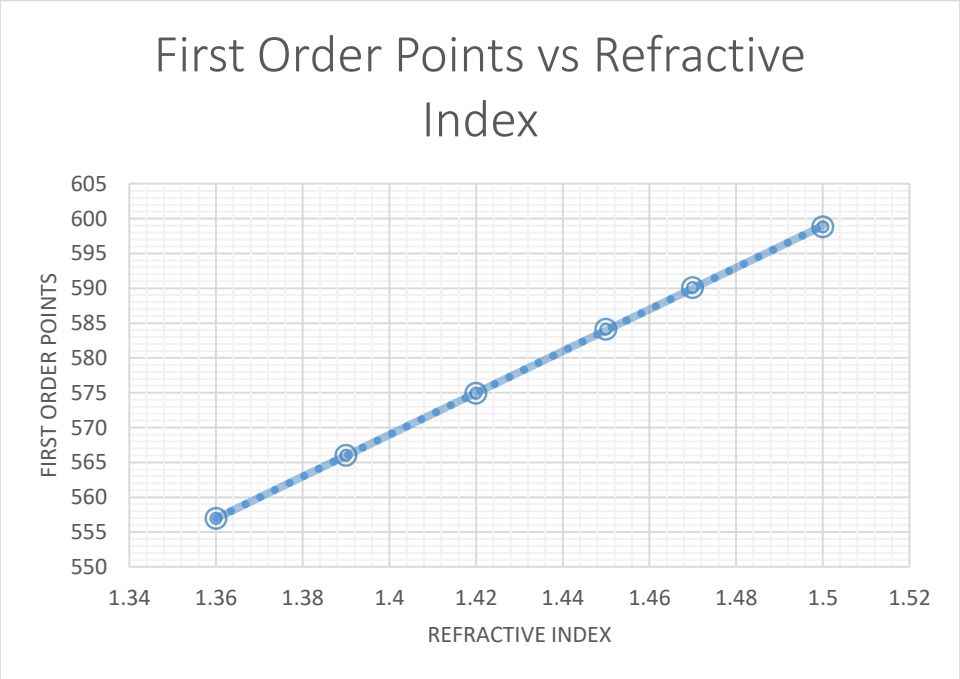

Figure 5.23 Sensitivity

Sensitivity is calculated by this formula: $d\lambda / dn$

Where,

dn= Change in refractive index

$d\lambda$ = Change in wavelength of incident light

Calculation:

Sensitivity is calculated from the slope of the curve

Sensitivity = (598.8-556.92) / (1.5-1.36) = 299.89

5.5 Sensitivity analysis for bio-molecule proteins

For this section the refractive index of the surrounding medium was changed to match that of various biomolecule proteins in various buffer solutions while keeping the object dimensions and materials constant. We select the cube length to be 20 nm and sphere diameter to be 25 nm and the materials for both to be silver. The source wavelength range is 500 nm to 600 nm and the number of frequency points to 500. The simulated biomolecules were Human Immunoglobulin G (IgG), Human fibrinogen (Fb), Human Serum Albumin (HSA) and Lysozyme (Lys). The first order points are recorded and the difference between the first Order points for all of the refractive indexes and the control group water is calculated. The corresponding values of the wavelengths are recorded and a graph of Wavelength vs. Refractive Index is plotted. The slope of the curve gives us the value of Sensitivity.

The refractive indices used in the simulation matched that of the four biomolecules mentioned above each placed in the buffer solutions mentioned below:

1. 40 microgram/mL HEPES
2. 80 microgram/mL HEPES
3. 6M Urea

HEPES is a widely used zwitterionic organic chemical buffering agent with the IUPAC name 2-[4-(2-hydroxyethyl)piperazin-1-yl]ethanesulfonic acid. Urea was simulated as well because it has a tendency to denature proteins [19] (causing their shape to change). This should cause a change in the way the proteins bind to the nanoparticle surface thus causing a change in the localised surface plasmon resonance (LSPR), possibly decreasing the LSPR shift for each biomolecule. This decrease in LSPR shift would mean that the biosensor is less sensitive therefore less effective. One of the purposes of this paper was to see whether our biosensor

would have a high enough sensitivity value that it would be able to overcome the denaturation by Urea.

5.5.1 40 microgram/mL HEPES

Water acts as the control medium. All the other media consist of a biomolecule mixed with 40 µg/mL HEPES.

Medium	Refractive Index, n	Wavelength/nm	LSPR shifting/nm
Water	1.33	547.97	0.000
Fb	1.39	565.974	18.004
IgG	1.41	572.029	24.059
HSA	1.45	584.081	36.111
Lys	1.50	598.8	50.83

Table 5.5 First Order Points and LSPR shifting vs Refractive Index for 40 microgram HEPES

Graphical Representation of Sensitivity:

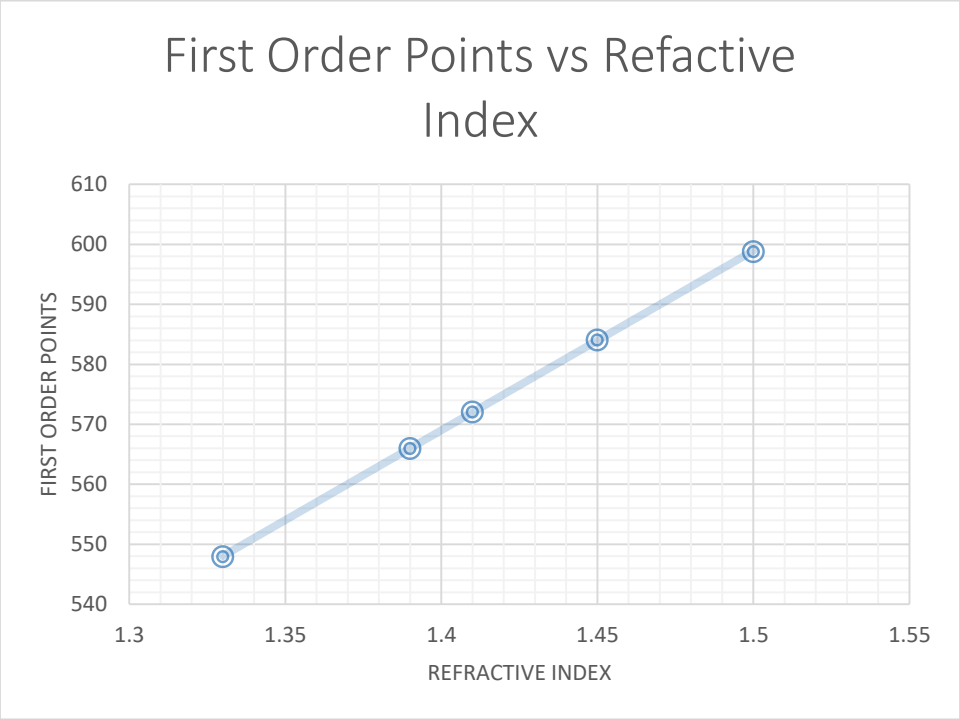

Figure 5.24 Sensitivity of 40 microgram HEPES

Calculation:

Sensitivity is calculated from the slope of the curve

Sensitivity = (598.8-547.97) / (1.5-1.33) = 299.3282

Graphical Representation of LSPR Shift:

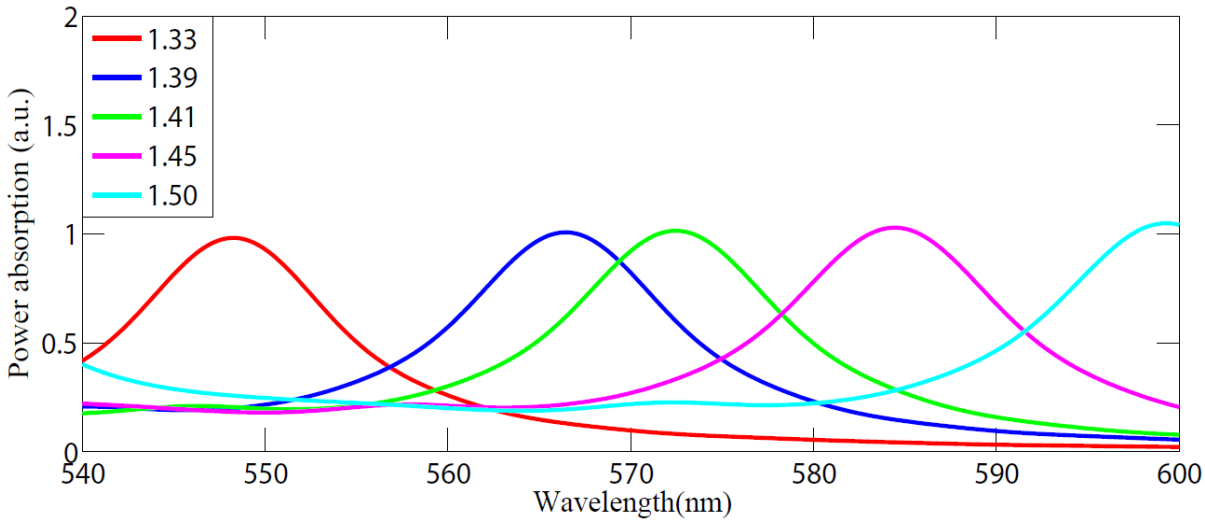

Figure 5.25 Power Absorption vs Wavelength for 40 microgram HEPES

5.5.2 80 microgram/mL HEPES

Water acts as the control medium. All the other media consist of a biomolecule mixed with 80 µg/mL HEPES.

Medium	Refractive Index, n	First Order Points/nm	LSPR shifting
Water	1.33	547.97	0.000
Fb	1.4	568.966	22.134
IgG	1.41	572.029	25.237
HSA	1.415	573.359	26.694
Lys	1.475	591.633	44.668

Table 5.6 First Order Points and LSPR shifting vs Refractive Index for 80 microgram HEPES

Graphical Representation of Sensitivity

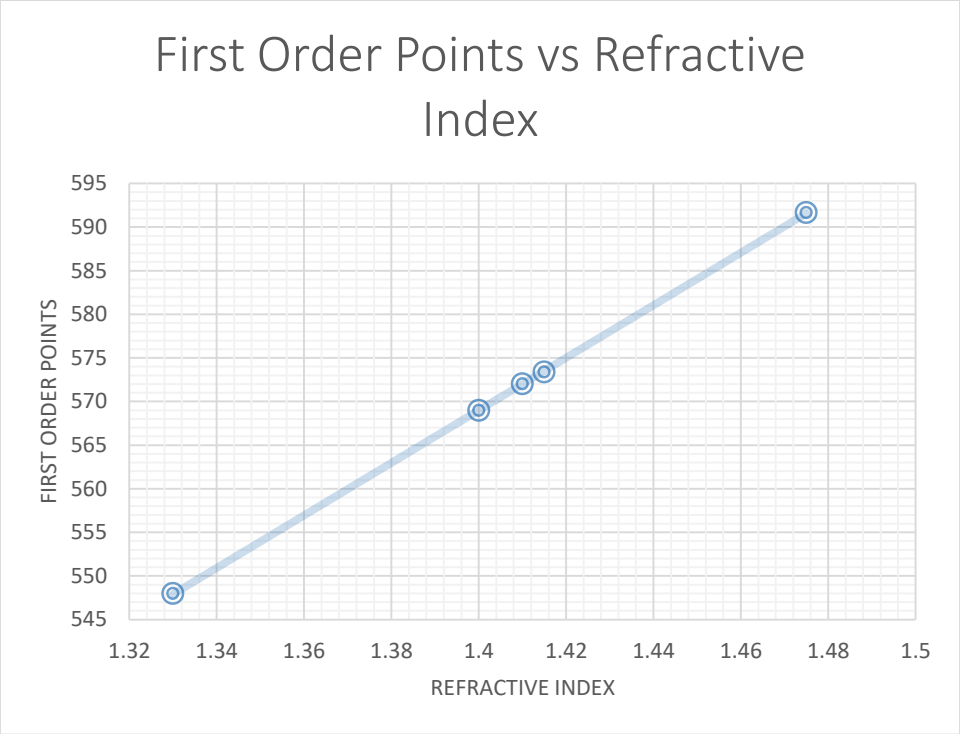

Figure 5.26 Sensitivity of 80 microgram HEPES

Calculation:

Sensitivity is calculated from the slope of the curve

Sensitivity = (591.633-547.97) / (1.475-1.33) = 300.9848

Graphical Representation

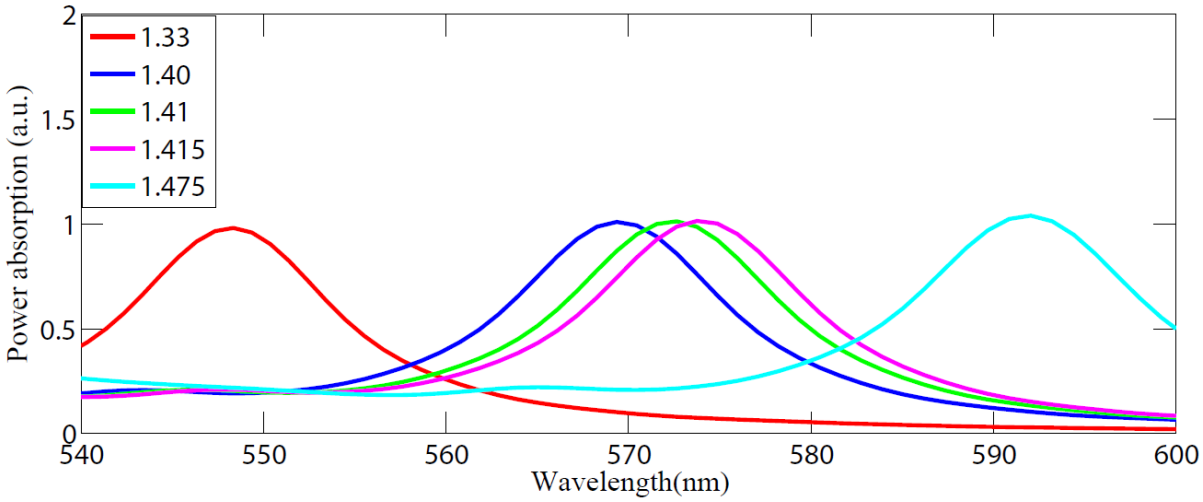

Figure 5.27 Power Absorption vs Wavelength for 80 microgram HEPES

5.5.3 6M urea

Water acts as the control medium. All the other media consist of a biomolecule mixed with 6M Urea.

Medium	Refractive Index, n	First Order Points/nm	LSPR shifting
Water	1.33	547.97	0.000
Fb	1.43	577.821	31.737
IgG	1.42	575.581	28.577
HSA	1.415	573.359	26.694
Lys	1.48	592.814	46.694

Table 5.7 First Order Points and LSPR shifting vs Refractive Index for 6M Urea

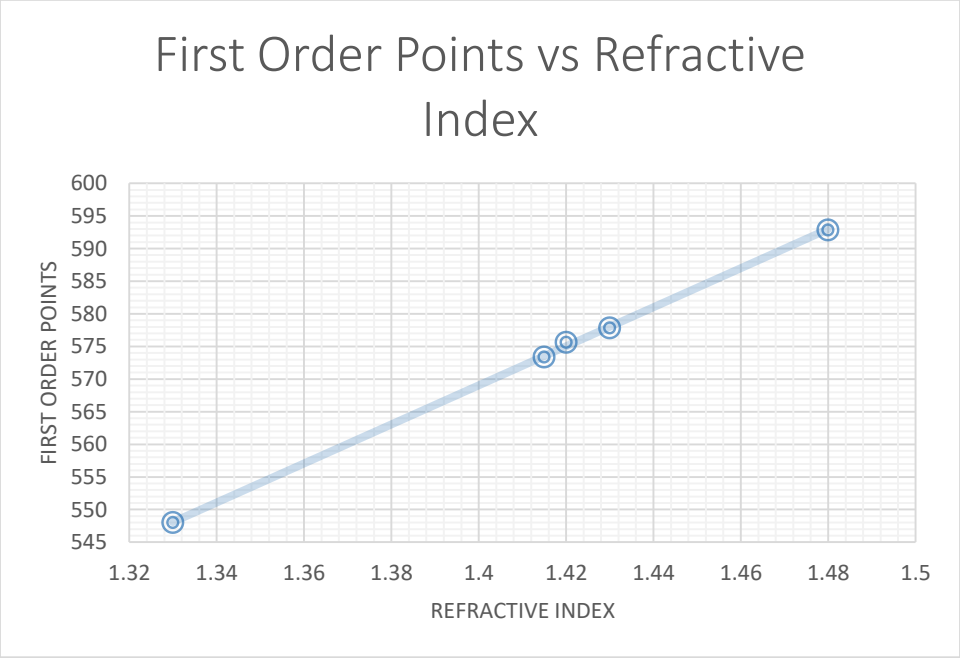

Figure 5.28 Sensitivity for 6M Urea

Calculation:

Sensitivity = (592.814-547.97) / (1.48-1.33) = 299.2034

Graphical Representation of LSPR Shift:

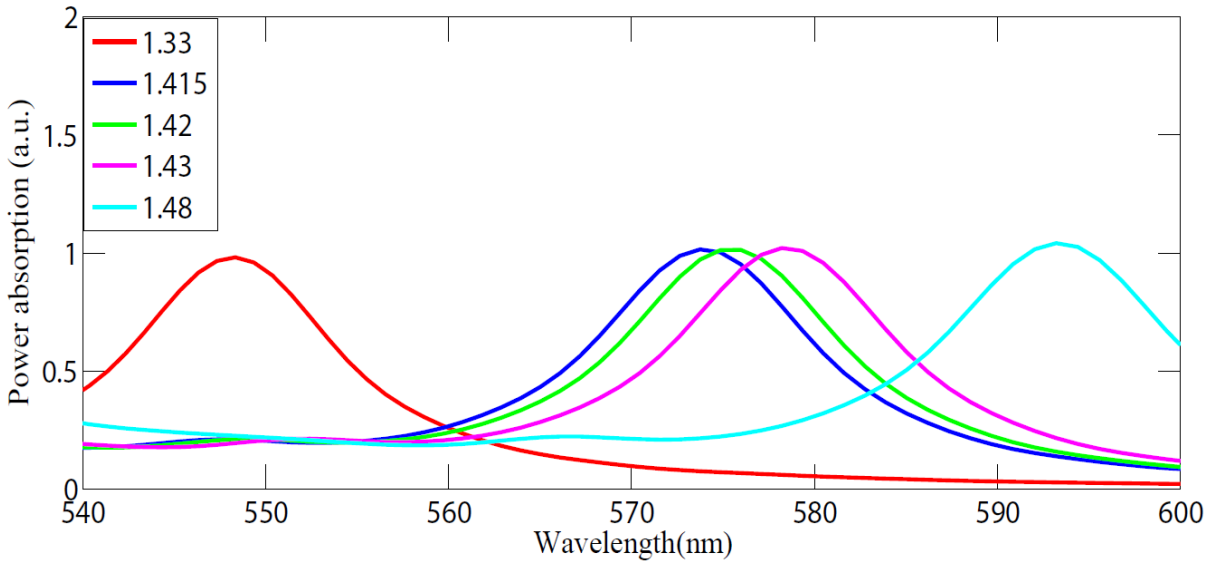

Figure 5.29 Power Absorption vs Wavelength for 6M Urea

6. Conclusion

This paper was done in the hopes of following the unique characteristics of Localized Plasmon Resonance (LSPR) in metallic nanoparticles. With its various applications in optics, photo catalysis, medicine and photovoltaic, our focus was on its application in bio sensing. The nanoparticles, cube and sphere were placed on a substrate (Silicon Dioxide). The setup was immersed in water and illuminated with light. As it is total field scattered field (TFSF), the light will fall on structure equally everywhere.

Here our research was based on the Power absorption and Electric field coupling of First Order Ordinary Plasmon Resonances. The results and analysis of our thesis was categorized into five sub-topics: “Materials”, “Gap change”, “Physical dimension”, “Sensitivity analysis” and “Sensitivity for biomolecules”.

“Materials” analysis was carried out for four different combinations of materials for the nanocube and nanosphere which were Au-Au, Au-Ag, Ag-Au and Ag-Ag. The substrate used for this analysis was Silicon Dioxide and the surrounding medium was water. Finally, the setup was illuminated with TSFS light. Initially we took a wavelength range of 100 nm to 900 nm and then classified the simulation again into various wavelengths depending on the multiple first order points. For these particular conditions, we observed the power absorption curve and the electric field coupling and based on that the Ag-Ag combination was selected.

Taking an Ag-Ag combination of constant size and other parameters, we varied the gap between them to see what value would give us the best power absorption curve and electric field coupling profile which ended being 1 nm so this gap magnitude was used for the remainder of the analyses.

“Physical dimension” was carried out similarly, the substrate and the surrounding medium remained the same. Initially radius of nanosphere was fixed and the length of nanocube was varied then the length of nanocube was fixed and radius of nanosphere was varied. After illumination and simulation, we obtain the power absorption curve and the electric field coupling. We observed the power absorption shifting with change of physical dimension. Based on power absorption shifting, we select one structure (NC-20 nm, NS-12.5 nm) for the rest of the paper.

For the “Sensitivity analysis” we took various common refractive indices, noted wavelength from first order points (wavelengths at which we get maximum power absorption) and calculated sensitivity. The sensitivity was found by calculating the slope of the graph of first order points vs refractive index.

The final portion was the "Sensitivity analysis for biomolecules". When biomolecules are placed in certain buffer solutions they have very specific refractive indices which can be used to simulate their presence so that is what was done here using the FDTD solutions software.

The buffer solutions were 40 microgram/mL HEPES, 80 microgram/mL HEPES and 6M Urea each of which held the biomolecules Lysozyme, Human Serum Albumin, Human Fibrinogen and Human Immunoglobulin G. For each buffer solution the sensitivity was found by calculating the slope of the graph of first order points (wavelengths at which we get maximum power absorption) vs refractive index. The sensitivity values for 40 µg/mL HEPES, 80 µg/mL HEPES and 6M Urea were 299.3282, 300.9848 and 299.2034 respectively. The 6M Urea solution having a sensitivity value of 299.2034 was surprising given that Urea causing the biomolecules to denature should have gotten us a much lower value but since it did not, this indicates that our setup had conditions and parameters so optimal that it was able overcome the denaturing phenomenon showing that it is an effective biosensor.

References

1. Chin, C. W., (2011). Localized Surface Plasmon Resonance with the use of Silver and Titanium Oxide Nanostructures. p. 1. Retrieved from:[2] http://web.utk.edu/~zzhang24/Chuck%20Chin%20Thesis.pdf

2. Stockman, M. I., (2011). Nanoplasmonics: the physics behind the applications. *Physics Today*, 39-44. Retrieved from:[4] http://physics.gsu.edu/stockman/data/Stockman_Phys_Today_2011_Physics_behind_Applications.pdf

3. Maier, S. A. (2007) Localized Surface Plasmons. *Plasmonics: Fundamentals and applications*, p. 65-72. Retrieved from:[5] https://www.london-nano.com/sites/default/files/uploads/research/highlights/Nanoplasmonics.pdf

4. Plasmonics. Retrieved from:[6] https://www.physik.hu-berlin.de/de/nano/lehre/Gastvorlesung%20Wien/plasmonics

5. Raether, H. (1988). Surface Plasmons on Smooth and Rough Surfaces and on Gratings[8]. *Springer Tractsin ModernPhysics*, Vol. 111, Springer Berlin

6. Localized Surface Plasmon Resonance Theory. *Localized Surface Plasmon Resonance vs. Surface Plasmon Resonance*. Retrieved from[9]: https://nicoyalife.com/technology/surface-plasmon-resonance/localized-surface-plasmon-resonance-theory/

7. Vörös, J. (2004). The density and refractive index of adsorbing protein layers. *Biophysical journal*, *87*(1), 553-561.

8. Colvin, J. R. (1952). The size and shape of lysozyme. *Canadian Journal of Chemistry*, *30*(11), 831-834.

9. Torsteinsdóttir, I., Håkansson, L., Hällgren, R., Gudbjörnsson, B., Arvidson, N. G., & Venge, P. (1999). Serum lysozyme: a potential marker of monocyte/macrophage activity in rheumatoid arthritis. *Rheumatology*, *38*(12), 1249-1254.

10. Sugio, S., Kashima, A., Mochizuki, S., Noda, M., & Kobayashi, K. (1999). Crystal structure of human serum albumin at 2.5 Å resolution. *Protein engineering*, *12*(6), 439-446.

11. Yike, I., Distler, A. M., Ziady, A. G., & Dearborn, D. G. (2006). Mycotoxin adducts on human serum albumin: biomarkers of exposure to Stachybotrys chartarum. *Environmental health perspectives*, 1221-1226.

12. Caspary, E., & Kekwick, R. A. (1957). Some physicochemical properties of human fibrinogen. *Biochemical Journal*, *67*(1), 41.

13. Selmeci, L., Székely, M., Soós, P., Seres, L., Klinga, N., Geiger, A., & Acsády, G. (2006). Human blood plasma advanced oxidation protein products (AOPP) correlates with fibrinogen levels. *Free radical research*, *40*(9), 952-958.

14. Hamilton, R. G. (1987). Human IgG subclass measurements in the clinical laboratory. *Clinical Chemistry*, *33*(10), 1707-1725.

15. Skyllouriotis, P., SKYLLOURIOTIS-LAZAROU, M., Natter, S., Steiner, R., Spitzauer, S., Kapiotis, S., ... & Wollenek, G. (1999). IgG subclass reactivity to human cardiac myosin in cardiomyopathy patients is indicative of a Th1-like autoimmune disease. *Clinical & Experimental Immunology*, *115*(2), 236-247.

16. PML boundary conditions. Retrieved from: https://kb.lumerical.com/en/index.html?ref_sim_obj_symmetric_anti-symmetric.html

17. About FDTD Solutions. Retrieved from: https://www.lumerical.com/tcad-products/fdtd

18. Power absorption per unit volume. Retrieved from: https://kb.lumerical.com/en/layout_analysis_pabs.html

19. Bennion, B. J., & Daggett, V. (2003). The molecular basis for the chemical denaturation of proteins by urea. *Proceedings of the National Academy of Sciences*, *100*(9), 5142-5147.